QUANTUM TUNNELING, QUANTUM COMPUTING, AND HIGH TEMPERATURE SUPERCONDUCTIVITY

A Dissertation

by

QIAN WANG

Submitted to the Office of Graduate Studies of
Texas A&M University
in partial fulfillment of the requirements for the degree of

DOCTOR OF PHILOSOPHY

December 2003

Major Subject: Physics

QUANTUM TUNNELING, QUANTUM COMPUTING, AND HIGH TEMPERATURE SUPERCONDUCTIVITY

A Dissertation

by

QIAN WANG

Submitted to Texas A&M University
in partial fulfillment of the requirements
for the degree of

DOCTOR OF PHILOSOPHY

Approved as to style and content by:

Chia-Ren Hu (Chair of Committee)	Glenn Agnolet (Member)
Vitaly Kocharovsky (Member)	Philip B. Yasskin (Member)
Edward S. Fry (Head of Department)	

December 2003

Major Subject: Physics

ABSTRACT

Quantum Tunneling, Quantum Computing, and High Temperature Superconductivity. (December 2003)

Qian Wang, B.S., Peking University;

M.S., Peking University;

M.S. Texas A&M University

Chair of Advisory Committee: Chia-Ren Hu

In this dissertation, I have studied four theoretical problems in quantum tunneling, quantum computing, and high-temperature superconductivity.

1. I have developed a generally-useful numerical tool for analyzing impurity-induced resonant-state images observed with scanning tunneling microscope (STM) in high-T_c superconductors. The integrated tunneling intensities on all predominant sites have been estimated. The results can be used to test the predictions of any tight-binding model calculation.

2. I have numerically simulated two-dimensional time-dependent tunneling of a Gaussian wave packet through a barrier, which contains charged ions. We have found that a negative ion in the barrier directly below the tunneling tip can deflect the tunneling electrons and drastically reduce the probability for them to reach the point in the target plane directly below the tunneling tip.

3. I have studied an infinite family of sure-success quantum algorithms, which are introduced by C.-R. Hu [Phys. Rev. A **66**, 042301 (2002)], for solving a generalized Grover search problem. Rigorous proofs are found for several conjectures made by Hu and explicit equations are obtained for finding the values of two phase parameters which make the algorithms sure success.

4. Using self-consistent Hartree-Fock theory, I have studied an extended Hubbard model which includes quasi-long-range Coulomb interaction between the holes (characterized by parameter V). I have found that for sufficiently large V/t, doubly-charged-antiphase-island do become energetically favored localized objects in this system for moderate values of U/t, thus supporting a recent conjecture by C.-R. Hu [Int. J. Mod. Phys. B **17**, 3284 (2003)].

To My wife, Ling Zhou

ACKNOWLEDGMENTS

It is impossible to come up with a list of individuals who have inspired, encouraged and helped in this achievement; however, I will try to list those who have served as guideposts along my path. My sincerest apologies for any oversights that I may make in this attempt as I take the risk of omitting those who deserve at least partial credit for this work.

First, I would like to express my gratitude to my adviser, Dr. Chia-Ren Hu, for his guidance and patience. I would also like to thank the rest of my committee for their endurance and patience. They are Dr. Glenn Agnolet, Dr. Vitaly Kocharovsky and Dr. Philip B. Yasskin.

Texas A&M University Physics Department is also gratefully acknowledged.

Finally, I wish to thank my parents and my wife for their love, encouragement, understanding and patience.

TABLE OF CONTENTS

CHAPTER Page

LIST OF FIGURES

FIGURE Page

FIGURE Page

FIGURE Page

CHAPTER I

GENERAL INTRODUCTION

In this dissertation, I will investigate several theoretical problems in the general areas of quantum tunneling, quantum computing, and high-temperature superconductivity. These problems are only loosely tied to each other in that they all involve some aspects of quantum mechanics.

This dissertation is organized as follows: In Chap. II, I will develop a generally-useful numerical tool for analyzing impurity-induced resonant-state images observed in high-T_c superconductors. Scanning with a low-temperature scanning tunneling microscope (STM) on a cleaved $Bi_2Sr_2CaCu_2O_8$ single crystal at a fixed bias energy, Pan et al. of the UC Berkeley group led by Professor Seamus Davis (now at Cornell University) observed images localized near individual Zn (zinc) impurities in the top-most CuO_2 plane [1], when the bias voltage is set at the peak of a near-zero-energy resonant. Using a numerical analyzing tool developed in this dissertation, I will analyze the set of data associated with each such image and convert it to a discrete set of integrated intensities one for each lattice site of a simple square lattice, which has been the basis of several tight-binding-type theoretical calculations, so that the different theoretical predictions can be compared with the experimental data.

In Chap. III, I will investigate two-dimensional transversely-localized quantum tunneling through a barrier which contains localized charges. I will numerically simulate such a two-dimensional tunneling process by solving the time-dependent Schrödinger equation to see how a wave-packet moves through a tunneling barrier containing a space-dependent barrier potential generated by one or more ions in the

---

The journal model is Physics Review B.

barrier, which will deform the wave-packet and its tunneling path. The purpose is to obtain some qualitative support for a "blocking model" proposed by Zhu, Ting, and Hu [2] for explaining the resonant-state STM images observed near Zn impurities in $Bi_2Sr_2CaCu_2O_8$ by Pan et al. [1]

In Chap. IV, I will study a family of sure-success quantum search algorithms, as a generalization of Grover's quantum search algorithm, proposed by Hu [3]. I will give rigorous proofs on several conjectures made by Hu, and also to extend his work in determining the explicit values of two adjustable parameters that make all members of the family sure-success algorithms.

In Chap. V I will study an extended Hubbard model in a square lattice, taking into account the Coulomb repulsion between holes. I will apply self-consistent Hartree-Fock approximation to study this model with the main purpose being the search for doubly-charged antiphase island, which is the main idea underlying a new mechanism for high-T_c superconductivity proposed by Hu. [4]

CHAPTER II

A GENERALLY-USEFUL NUMERICAL TOOL FOR ANALYZING IMPURITY-INDUCED RESONANT-STATE STM IMAGES OBSERVED IN HIGH-T_C SUPERCONDUCTORS

A. Introduction

Scanning a Low-Temperature STM on a cleaved $Bi_2Sr_2CaCu_2O_8$ single crystal at a fixed bias energy, Pan et al. of the UC Berkeley group led by Professor Seamus Davis (now at Cornell University) observed images localized near individual Zn impurities in the topmost CuO_2 plane,[1] when the bias voltage is set at the peak of a near-zero-energy resonance. A typical such image is shown in Fig. 1.

Understanding this resonant-state image is a great challenge. Due to the past several years of experimental and theoretical studies, it has been widely accepted that high-T_c superconductors have a $d_{x^2-y^2}$-wave pairing symmetry. [5] This type of d-wave symmetry differs from a conventional s-wave symmetry in the following feature: A gap function (or pair potential) with this symmetry has line nodes parallel to the c-axis along the $\{11\}$, $\{1\overline{1}\}$, $\{\overline{1}1\}$, and $\{\overline{11}\}$ directions in the ab plane on an essentially cylindrical Fermi surface of a high-T_c superconductor, and changes sign across any of these nodal lines, whereas if it had an s-wave symmetry the gap function would have a constant sign everywhere on the Fermi surface. Many theorists have shown that a unitary impurity in a d-wave superconductor can induce the formation of two essentially degenerate resonant states per spin of almost zero energy which are quasi-bound to the impurity. The predicted spectral peak-feature near zero bias [6] agrees with observations very well [7], but the predicted resonant-state STM image based on the wave functions of these resonant states only differs dramatically from the observed

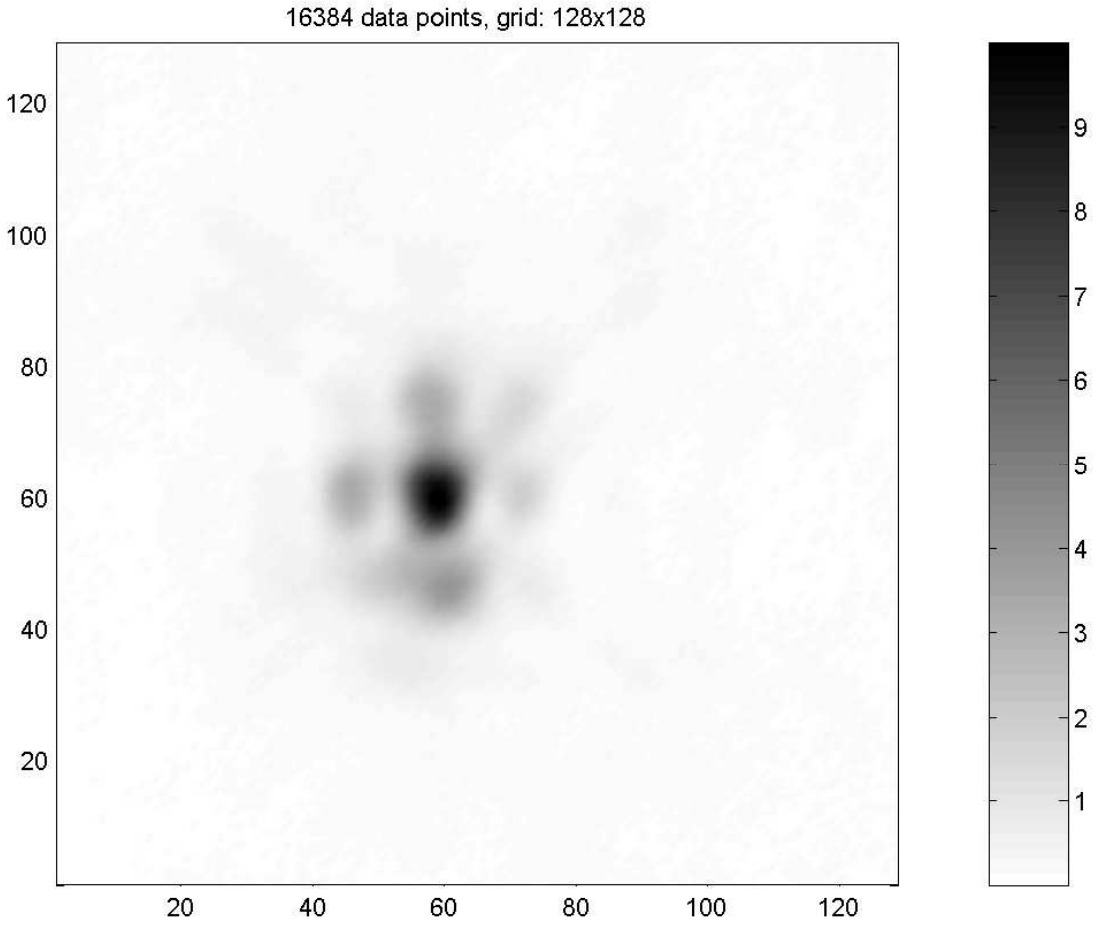

Fig. 1. A typical resonant-state STM image given in Ref. [1] near a Zn impurity in the topmost CuO_2 plane of a cleaved single crystal of $Bi_2Sr_2CaCu_2O_8$ below T_c, when the bias voltage is set at the peak of a near-zero-energy resonance. The a and b crystal axes are essentially along the diagonals in this figure.

ones. For example, Ref. [2] has given such an image as shown in Fig. 2. This figure shows a vanishing intensity at the unitary impurity site and largest intensities at the four nearest-neighbor sites. This is in sharp disagreement with the observation shown in Fig. 1, where the largest intensity is at the center (impurity) site, and nearly vanishing intensities at the four nearest-neighbor sites. This disagreement is a model-independent conclusion, since a resonant-state wave function must vanish at the site of a unitary impurity, and a non-unitary impurity can not give a near zero-energy resonance. The disagreement also extends to the second and third nearest neighbor sites, where both the measured and calculated intensities are not small. Two theories have been offered to explain this disagreement [2, 8]. Both theories are of tight-binding nature. Namely, tunneling intensities are predicted at the Zn or Cu sites only, with no continuous intensity distribution between these lattice sites. This is of course not what has been observed, which is quasi-continuous, as is shown in Fig. 1. Thus to compare experimental data with these theories, it is necessary to convert the measured data to a set of discrete tunneling intensities at the Cu or Zn sites, by performing some sort of integration.

Each set of experimental data provided by Seamus Davis group has two STM images. One is a topographic image (an energy-integrated spatial image), which gives the top BiO layer with only the Bi atoms showing in it. The atoms are observed to be displaced from their ideal orthorhombic lattice sites, forming a supermodulation with a wave vector along the b-axis. According to the crystal structure of $Bi_2Sr_2CaCu_2O_8$ Bi atoms are above the Cu atoms (or the Zn atoms which are impurity atoms substituting for Cu atoms). The other image, such as shown in Fig. 1, is taken with STM in the same local area, but with the bias voltage set essentially at the peak of a near-zero-energy resonance. The higher resolution data taken are made of 128×128 intensity points. Each bright spot in the Fig. 1 spreads about 5 points in each direc-

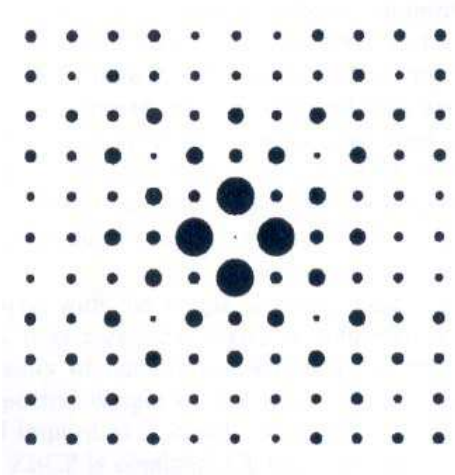

Fig. 2. The predicted resonant-state image near a unitary impurity in a d-wave superconductor based on the resonant-states wave functions only, as is given in Ref. [2].

tion. The spread of each spot is due to at least two effects, electron wave function and thermo-smearing. These bright spots are seen to spread into and overlaps with each other. That is, contribution from one Cu(Zn) site tails into neighboring sites. Thus to simply integrate the tunneling intensity over a unit-cell region around each lattice site can not give a correct estimate. We have thus developed a generally-useful numerical tool for estimating the integrated intensity associated with each lattice site around an impurity.

The chapter is organized as follows. In Sec. B, we present the numerical procedure for analyzing these resonant-state images. The results obtained from these images will be given in Sec. C, which also contains a short conclusion.

B. Method

We assume that the tunneling intensity contributed by a single Cu(Zn) site has a generalized Gaussian form. We make this assumption for the following three reasons.

First, we do not know the exact form of the contributing electronic wave function at the present time. The electron wave function at a Cu site is $d_{x^2-y^2}$, but tunneling might be via some higher s-wave orbitals. Besides, this $d_{x^2-y^2}$ orbital should presumably still hybridize with the nearest Oxygen p_x or P_y orbitals. [9] There are also two more atomic layers above the topmost CuO_2 plane, a BiO plane and a SrO plane. The BiO plane, the topmost layer, is believed to be semiconducting, whereas the SrO plane, the second layer, insulating. Ions residing on these upper two layers may interfere with the measurement of any state in the CuO_2 plane. Secondly, if thermo-smearing effect dominates, the spreading of each spot presumably should take a Gaussian form. Experimental limitations in resolution should presumably also be modeled by Gaussian functions. Thirdly, the generalized Gaussian function is the simplest form we can use which can take into account many features of the peaks in the observed data, such as position, intensity, width, anisotropy, orientation, etc. In addition, the more accurate data that are provided to us for analysis are taken on 128×128 points, and the radius of each bright spot covers about 5-points by 5 points. If we use a more complicated function to model the contribution from each lattice site, the number of estimated parameters may be too large. Then we may not be able to determine all parameter values accurately from the given data.

We thus assume that the tunneling intensity peak at each site i takes the form of the generalized Gaussian function $I(x,y) = \exp(a_{1i}+a_{2i}x+a_{3i}y+a_{4i}x^2+a_{5i}xy+a_{6i}y^2)$, where a_{ji}, $j = 1$ to 6, are parameters to be estimated, the total number of parameters is 6 times the number of peaks (which is an input by the user, and should be larger than the number of predominant peaks). After obtaining the parameters of these Gaussian functions, the integrated intensity at site i can be easily shown to be:

$$I_i = 2\pi \frac{\exp\left(a_{1i} - \frac{a_{5i}a_{2i}^2 + a_{4i}a_{4i}^2 - a_{6i}a_{2i}a_{3i}}{4a_{4i}a_{5i} - a_{6i}^2}\right)}{\sqrt{4a_{4i}a_{5i} - a_{6i}^2}} \tag{2.1}$$

for $a_{3i} < 0$, $a_{4i} < 0$, and $a_{5i}^2 - 4a_{3i}a_{4i} < 0$. Otherwise the integrated intensity at this site will be taken as zero. (These inequalities ensure that the generalized Gaussian is not pathological.)

We use an iterative procedure to estimate the parameters of these Gaussian functions. The procedure is as follows:

1. Initialize all the parameters so that each peak intensity is very small. This can be easily done by setting each a_{1i} negative and large.

2. Let $i = 1$, which refers to the highest peak in the data under analysis.

3. From the measure data, subtract out all contributions from all Gaussian peaks other than i. This step initially does little change to the measured data, but in later iterations, it will subtract out all Gaussian peaks already found.

4. Gaussian fit the remaining data around the highest point, and obtain 6 parameters for the peak i. The fitting region is taken to be somewhat smaller than a unit cell, since the weak-intensity region is more likely influenced by the neighboring contributions. When conditions $a_{3i} < 0$, $a_{4i} < 0$, and $a_{5i}^2 - 4a_{3i}a_{4i} < 0$ are not met, we set a_{1i} negative and large, so it is not considered a peak and will not be subtracted in the following iterations.

5. Let $i = i + 1$, which refers to the next highest peak in the data under analysis (obtained with a simple computer search), and go back to step 3.

6. Continue this procedure as long as $i \leq$ the input number of peaks.

7. Repeat 2 through 6 several times in order to improve the separation of the individual peak contributions. Stop iteration when the so-obtained parameter

values stop changing within a given accuracy. Usually three to four iterations are sufficient.

C. Results and Conclusion

We have analyzed three higher-resolution resonant-state images, each taken on 128x128 points around a Zn site. Several images given to us are taken on 64x64 points, which we are unable to analyze, because the number of data points available to estimate the 6 parameters of each Gaussian function is too small. We set the input number of peaks to be 15, which is larger than the number of the predominant peaks, which is about 9. The total number of fitting parameters is then 90. We believe that without the scheme devised here, it wouldn't be possible to determine so many fitting parameters accurately. If only higher resolution data could become available in the future, we think that this input number can still be increased to include the weaker peaks, thereby allowing more stringent tests of theories.

Fig. 3 shows the density plot of the fitted image we have obtained from the actual STM image shown in Fig. 1. Comparing the two images, we can see that the fitted image gives all predominant peaks and looks very similar to the actual image. For more detailed comparison we have plotted in Figs. 4 the fitted data and the actual STM data along a vertical line and a horizontal line (in the (11) and $(1\bar{1})$ crystal directions) that pass through the central peak. We have also plotted in Figs. 5 the fitted data and the actual STM data along two diagonal lines (in the (01) and (10) crystal directions) that pass through the central peak. We can see that the fitting is very good, although there are still some discrepancies. The position, width and height of each fitted peak are seen to be very close to those of the actual data.

We have applied our method on three sets of 128×128 STM image data pro-

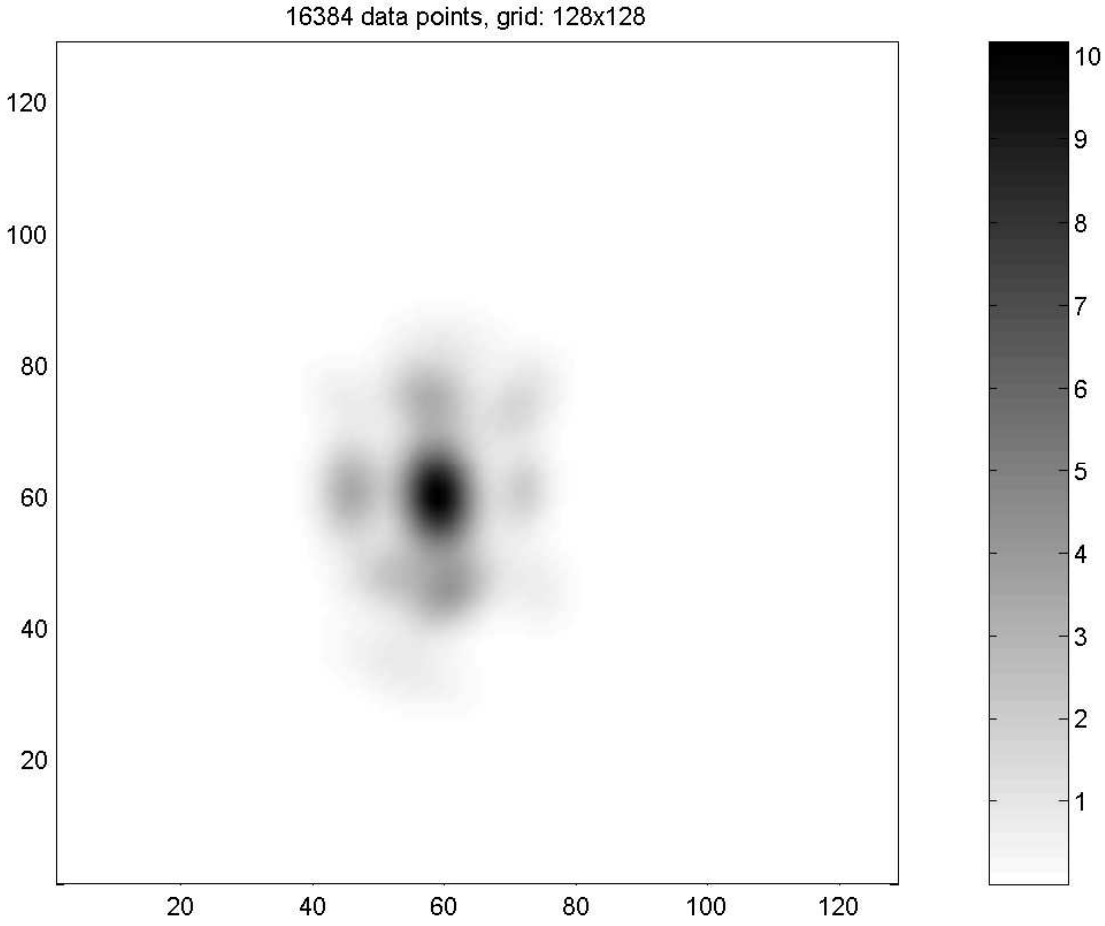

Fig. 3. Density plot of a fitted image obtained from the observed image shown in Fig. 1. The input peak number has been taken as 15. Thus it can only reproduce the 15 most predominant peaks in the actual STM image.

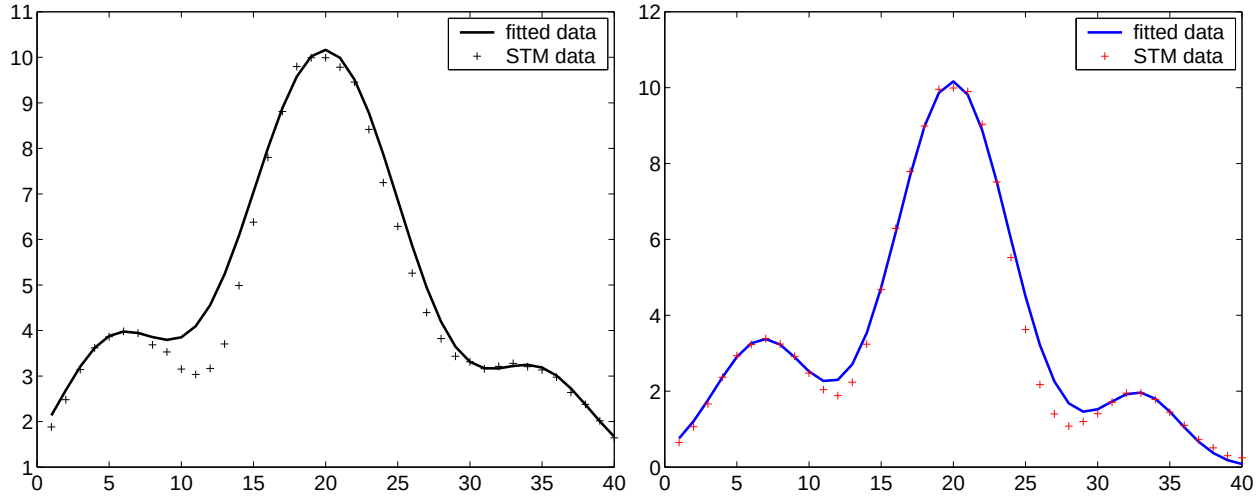

Fig. 4. Fitted data and the actual STM data along a vertical (left) and a horizontal (right) line which pass through the central peak. Solid lines represent the fitted behavior; the + symbols represent the actual STM data.

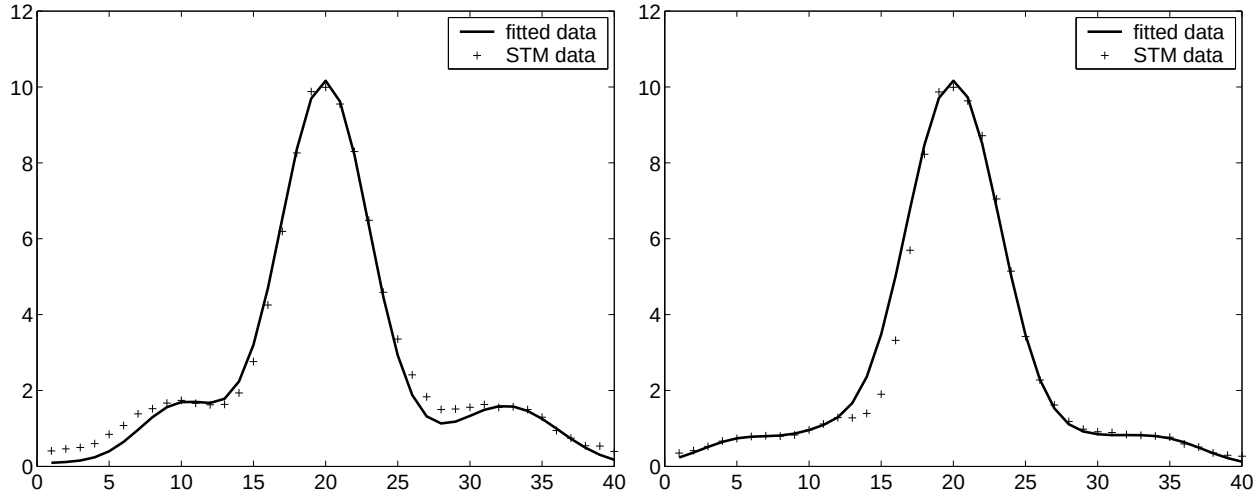

Fig. 5. Similar to the previous figure, except that the fitted data and the actual STM data are along two diagonal lines (i.e., in the 10 and 01 crystal directions,) which pass through the central peak.

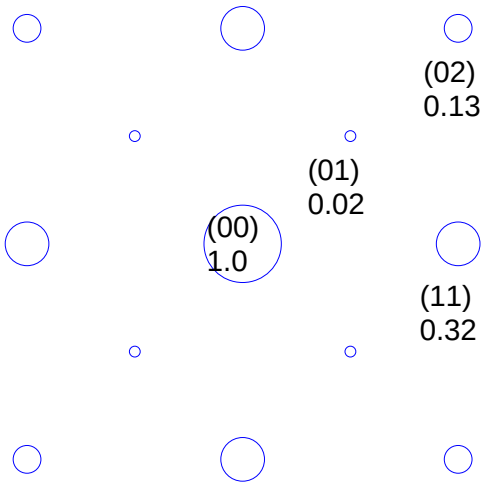

Fig. 6. Integrated tunneling intensities normalized to unity at the central peak extracted from our analysis. They are: 1.0 at the (00) site, 0.02 at the (01) sites, 0.32 at the (11) sites, and 0.13 at the (02) sites. These results have been averaged over three sets of data and also over all equivalent sites to restore perfect square symmetry.

vided to us and have obtained from them the averaged integrated relative tunneling intensities, which are normalized to unity at the center (Zn-impurity) site. (We have found that many 64×64 data sets provided to us do not have the resolution needed for this analysis. There are also two 128×128 data sets which correspond to a different type of resonant-state image. We have not included them in our determination of the averaged, integrated, relative tunneling intensities, because we suspect that they may correspond to a Zn impurity in a different local environment.) The average is done over the three usable images provided to us and also over all equivalent sites in each image to restore square symmetry — For example, average over the (01), (10), $(0\bar{1})$, and $(\bar{1}0)$ sites is reported as the result for all these four sites. It is to remove features unique to any single image and also features so far not taken into account in theories. The results are shown in Fig. 6, with the relative intensities presented by the areas of the circles. These averaged, relative, integrated tunneling intensities are

1.00 at the (00) site, 0.02 at the (01) sites, 0.32 at the (11) sites, and 0.13 at the (02) sites. These values can be used to test the validity of any tight-binding-type theories of such images. For example, Ref [2] has provided such a theory which is based on a blocking model. In that work, a very crude comparison of the predicted values of that theory with the measured values at the lattice sites has been made. But as has been explained there, the measured tunneling intensity is a quasi-continuous function of position, rather than existing at the lattice sites only, so some sort of integration should be performed on the measured data before they could be compared with the predictions of any tight-binding type of theories. This is the main reason that this work is done, so in Table I we have made a new comparison. Row one of this table gives the measured data used in Ref [2] which is really incorrect because it didn't employ any spatial integration, but is simply the measured intensity at the lattice sites. It was used there for a very crude comparison between theory and experiment only. Row three gives the predicted values of Ref [2] based on a blocking model introduced there. The discrepancy between row one and row three can not be taken seriously for the reason already given in Ref [2], which has been repeated above. Row two of this table gives a set of integrated intensities obtained in this analysis. We see that the main difference between row one and row two is in the values at the (10) and (01) sites. Clearly this is because the tall central peak has tailed substantially to the (10) and (01) sites. This fact further supports the conclusion that row one should not be used for comparison with row three, revealing the necessity of this analysis. The discrepancy between row two and row three is much more likely to be a genuine discrepancy, and likely indicates that the model needs to be improved. Ref [8] did not provide such numbers for a similar comparison, but it should be done to test its validity.

In conclusion, we have developed a generally useful tool for analyzing impurity-

Table I. Comparison between the measured STM local tunneling intensities at the near-zero-bias resonant energy by Pan *et al.* [1], and the blocking-model predictions of Ref. [2], at the nearest neighbor sites (10) and (01), the next nearest neighbor site (11), and the third nearest neighbor sites (20) and (02), after normalizing both sets of data to unity at the Zn impurity site (00). The first row is the measured tunneling intensity at the lattice sites around the Zn impurity, used in Ref. [2] for crude comparison. It really should not have been used (as has been explained there), since the measured data is quasi-continuous, so some sort of integration should be performed in order to obtain the integrated tunneling intensities at the lattice sites, so it can be compared with predictions of tight-binding-type theories, such as the theory in Ref. [2]. The second row is such an integrated set of intensities obtained in the present analysis. The third row is the prediction of such intensities from Ref. [2] that is based on a blocking model introduced there.

(00)	(10) & (01)	(11)	(20) & (02)
1.00	0.18	0.29	0.13
1.00	0.02	0.32	0.13
1.000	0.068	0.593	0.384

induced resonant-state STM images observed in high-T_c superconductors. The main purpose of this analysis is to convert the actually observed quasi-continuous image to a discrete set of integrated intensities, one for a lattice site of a square lattice, so it can be compared with the predictions of those tight-binding-type theories of such an image which treat a CuO_2 plane as a simple square lattice for holes to reside on and hop around. This tool should also be useful for analyzing similar such images which might be observed in other systems, for a similar purpose. We assume that the resonant-state image observed by Pan et al. near a Zn impurity in high-T_c superconductor $Bi_2Sr_2CaCu_2O_8$ is made of a sum of n overlapping generalized Gaussian functions, one roughly located at a different lattice site of a 2D square lattice (but allowing possible shifts from the ideal lattice-site positions). An iteration procedure is introduced which allows the $6n$ parameters in the n generalized Gaussian functions to be determined. (n has been set as 15 so far, which is not expected to be the upper limit.) The fitted image is shown to agree very well with the experimentally observed image, as far as all prominent peaks are concerned. Normalized integrated tunneling intensities on all predominant sites can then be extracted from this fitted image by integrating each Gaussian function. They can be compared with predictions of any tight-binding-type theory which consider a CuO_2 plane as a simple square lattice. If higher resolution images could be obtained, we could replace the generalized Gaussian function used here with a more complicated model function to do such an analysis, such as using some atomic orbital(s), possibly hybridized, convoluted with thermal smearing. Thus this analysis has the potential of finding the correct single-site contribution, thereby revealing useful detailed information about the system. That here we found that generalized Gaussian functions can give excellent fits calls for theoretical understanding, but perhaps higher resolution data will reveal their inadequacy. Another potential usefulness of this tool is to uncover different local

environments for the impurity atoms. For example, a Zn impurity could be paired with an O or Bi vacancy straight above it, or an O or Sr vacancy to the side of those sites, or a missing O atom to the side of the Zn atom in the same CuO_2 plane, or even a pair or more of Zn impurities in proximity, etc. Discovering these combinations might provide additional information about the system and the underlying mechanism for high temperature superconductivity, and allow more stringent tests of theories on such images.

CHAPTER III

QUANTUM TUNNELING THROUGH A BARRIER CONTAINING LOCALIZED CHARGES

A. Introduction

Since its invention in 1982, Scanning Tunneling Microscopy (STM) has been proved to be a powerful tool for obtaining local structural information on metallic and semiconducting surfaces. In STM, an atomically sharp tip is brought to close proximity (usually a few Å) of a sample. Holding the bias voltage at some specific value, the tip is raster scanned at a distance over the sample surface, and tunneling current is measured to generate a real-space image.

STM and its related scanning probe techniques provide major challenges for a theoretical treatment. By starting with well-defined test structures, the experimentalists have verified that the real-space images, obtained by STM, correspond closely to the expected surface structures as deduced by using other experimental techniques. However, for the application of STM to previously unknown surface structures, a profound theoretical understanding is needed in order to relate the real-space images to the spatial variation of some physical properties of the samples under investigation.

Recently, STM has been applied to study layered structures, such as the experiment performed by Pan et. al [1] on cuprate high-T_c superconductors such as $Bi_2Sr_2CaCu_2O_8$. Unlike normal metallic and semiconductor surfaces, the superconducting layer under investigation (i.e., the topmost CuO_2 layer) of a cleaved single crystal of of high-T_c superconductor $Bi_2Sr_2CaCu_2O_8$ is not the topmost layer of the sample. Above it, there is first a top layer that is semiconducting (a BiO layer) and next a second layer that is an ionic insulating layer (a SrO layer). The potential in

the barrier is no longer a constant but is distorted by the ions in these layers (*i.e.*, Bi^{3+} and O^{2-} ions in the BiO layer and Sr^{2+} and O^{2-} ions in the SrO Layer). The experiment by Pan et al. leads to an apparent contradiction with other available information on the electronic structure of the layer under study. What Pan et al. observed is a "resonant state image" in the following sense: First of all, if the STM tip is fixed at a location near a Zn impurity in the topmost CuO_2 layer, and the tunneling conductance is measured as a function of bias voltage V, they do not observe a d-wave superconductor like density of states, as would be observed if the tunneling tip is far away from any impurity. Instead, they observe much weaker coherence peaks plus a tall and narrow resonance peak very close to zero bias. With the bias voltage fixed at this peak, they then scan the STM tip over an area many lattice-constants large centered around a Zn impurity, and observe a geometric image localized at this impurity. The largest peak of this observed "resonant-state image", as shown in Fig. 1, is found to be at the impurity site. Tunneling intensities at the four nearest-neighbor sites are nearly vanishing. Theoretical study shows that a unitary impurity in a d-wave superconductor can induce the formation of two very nearly degenerate resonant states (per spin) that are very near zero energy (relative to the Fermi energy). But the predicted image based purely on the resonant-states wave functions by many groups [10], including an extensive numerical modeling in Ref. [2], with result given in its Fig. 2, is very different from the observed one. One sees that the intensity rather vanishes at the impurity site and is largest at the four nearest-neighbor sites. This is a model-independent conclusion, since only a unitary impurity can generate a resonance state at near zero energy [10] (relative to the Fermi energy) in a d-wave superconductor, but the wave function of any state quasi-bound to a unitary scatterer must vanish at the impurity site. In Ref. [2], a phenomenological "blocking model" is then proposed to account for this serious discrepancy. The basic idea in this model is

that the transversely-localized tunneling current from the STM tip to any site in the topmost CuO_2 layer can be deflected by the Coulomb forces from localized ions in the BiO and SrO layers above the said CuO_2 layer. More precisely, straight above a Cu site, there is an O^{2-} ion in the SrO layer and a Bi^{3+} ion in the BiO layer. These are then the most important ions to deflect the tunneling current trying to reach the said Cu site from the tunneling tip straight above the said Cu site. Thus in the blocking model, it is proposed that the tunneling current is actually blocked from reaching the said Cu site, but will mainly reach the four nearest-neighbor sites.

The most widely used theory of STM was developed by Tersoff and Hamann[11]. It is a perturbative treatment of tunneling based on Bardeen's transfer Hamiltonian approach[12]. This method requires explicit expressions for the wave functions of the tip and the sample surface. Within this model, the tunneling conductance at low bias and low temperature is proportional to the local density of states of the unperturbed sample evaluated at the Fermi level and at the tip curvature center. This theory has allowed one to explain many STM phenomena such as the resolution of tunneling microscopy, the interpretation of STM images. However, we can not use this theory to explain these resonant-state images, because we do not know the expressions for the wave function of the sample surface. More than a decade has passed since the discovery of high-T_c superconductivity, its mechanism is still unknown. Thus we do not have the exact form of the wave function at the impurity site in $Bi_2Sr_2CaCu_2O_8$. Even if we knew the wave function in the superconducting layer, since there are other layers above the superconducting layer, one can not use it directly to calculate the density of states at the tip.

We therefore numerically simulate a two dimensional time-dependent scattering of a Gaussian wave packet through a barrier, which contains charged ions, and seek support for the blocking model proposed by Zhu, Ting, and Hu for explaining the

resonant-state images. [2] This simulation method has been used for investigating the distribution of the STM current through a nanostructured material. [13]

B. Method and Results

1. Gaussian wave packet

The wave function of a free particle can be described by a wave packet. In quantum mechanics, Heisenberg's uncertainty relation implies that one can not accurately measure the position and the momentum of a particle at the same time. The highest precision in measurement of position and momentum is obtained by taking Gaussian wave packet as the initial wave function. In Free space, a Gaussian wave packet moves much the same way like a classical particle. At time zero, the initial wave function of a three-dimensional Gaussian wave packet takes the form

$$\Psi_(\mathbf{r},0) = A\exp\left[\frac{-(\mathbf{r}-\mathbf{r_0})^2}{2\sigma(0)^2} + i\mathbf{k_0}\mathbf{r}\right], \tag{3.1}$$

where A is the normalization factor, $\hbar\mathbf{k_0}$ is the mean momentum, and $\mathbf{r_0}$ denotes the center of the wave packet. $\sigma(0)$ determines the spread of the initial wave packet. At later time t, $\sigma(t)$ increases with time from its minimum value $\sigma(0)$ and has the form $\sigma(t) = \sqrt{\sigma^2(0) + [\frac{\hbar t}{2m\sigma(0)}]^2}$.

2. Numerical simulation

In this work, we numerically simulate a two-dimensional, localized, tunneling process in STM by solving time-dependent Schrödinger equation to see how a wave packet moves through the space-dependent ionic potential generated by ions, which will deform the wave packet as well as its trajectory.

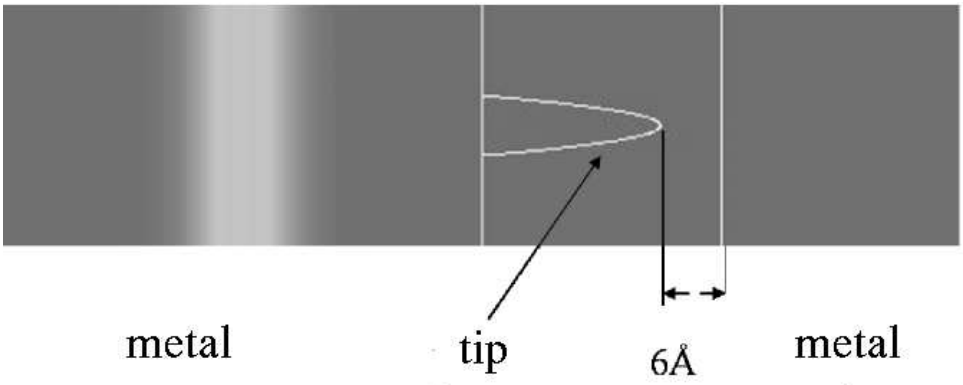

Fig. 7. Geometry of the two-dimensional tunneling problem solved here. The bright band denotes the incoming 1D wave packet.

We consider the problem of solving the one-body Schrödinger equation

$$H(\mathbf{r})\psi(\mathbf{r},t) = i\frac{\partial}{\partial t}\psi(\mathbf{r},t). \tag{3.2}$$

. For a local potential, the Hamiltonian has the form

$$H(\mathbf{r}) = T(\mathbf{r}) + V(\mathbf{r}), \tag{3.3}$$

where $T = -\frac{\hbar^2}{2m}\nabla^2$ and V($\mathbf{r}$) are the kinetic and potential energy operators. The quantum state is evolved forward in time by the Schrödinger evolution operator $\exp[-it(T+V)]$. Due to limitations in computer resourses, we are forced to consider a two-dimensional problem. Tunneling is considered to occur between two vertical metallic plates separated by a gap. The right plate represents the sample. A (two-dimensional) parabolic conducting region is added on the surface of the left plate to represent the tunneling tip, as shown in Fig. 7. The initial wave function in the left metallic plate is taken to be a wide one-dimensional Gaussian wave-packet localized only in the direction of propagation. When the wave emerges from the tip (and into the barrier), it will become two-dimensionally localized. (In actual tunneling situ-

ations it should be three-dimensionally localized.) Ions will be placed between the tip and the sample (i.e., inside the tunneling barrier). To Solve the time-dependent Schrödinger equation, the method developed by Chin and Chen [14] will be employed. The purpose of the study is to investigate how a tunneling wave-packet moves inside such a barrier in order to see whether there may be a distorted tunneling path due to the influence of the ionic potential inside the barrier. (Note that even though we have started with a one-dimensional wave packet, when it leaves the tunneling tip and enter the tunneling barrier it will form a three dimensionally localized wave packet which will then propagate across the tunneling barrier to reach the sample.) The wave function at time t can be obtained by applying the evolution operator for a very short time interval Δt repeatedly on the initial wave function. The problem with this procedure is that the evolution operator cannot be calculated exactly for a Hamiltonian given above, because T and V do not commute. It is therefore approximated by a factorization procedure $\exp[-i\Delta t\,(T+V)] \approx e^{-\frac{1}{2}i\Delta t\,V} e^{-i\Delta t\,T} e^{-\frac{1}{2}i\Delta t\,V}$. Since the kinetic energy operator is diagonal in momentum space, this approach shuffles the wave function back and forth between real and Fourier space. Every occurrence of $e^{i\Delta t\,T}$ requires two fast Fourier transforms, one direct and one inverse. This method has the advantage that the normalization is conserved, because $\exp[-i\Delta t\,(T+V)]$ in the above approximate form is unitary.

The parameters of the parabola modeling the tip are as follows: The width at its base is 6Å. Its height is 18Å. The height is much longer than the base so that most tunneling occurs through the tip of the parabola. The distance between the sample surface and the tip of the parabola is set at 6Å, which is close to the distance between the actual STM tip and the superconducting layer in $Bi_2Sr_2CaCu_2O_8$. We want to simulate a DC current. However it is impossible to study a true DC current in our method. So instead, our initial wave function is taken to be a wide one-dimensional

Gaussian wave packet $\Psi(x,y) = A\exp[-\frac{(x-x_0)^2}{4\sigma^2}]e^{ik_0x}$. The median wave vector is taken to be $k_0 = 3\text{Å}^{-1}$, which gives a Fermi velocity of 3.5×10^6m/s and corresponds to a mean energy of 34.38eV (the bare mass of an electron has been assumed. σ is taken to be 3.5Å. The barrier height is taken to be 50eV, to minimize the portion of the wave packet with energy above the barrier height. Thus this choice of the barrier height is artificial and is not really equal to any actual barrier height. It is adopted here to solve the problem just described, namely, we must work with a wave packet rather than a truly DC tunneling current, but any wave packet is a mixture of different wave numbers and therefore energies. We need to minimize the contributions of components with energies higher than the tunneling barrier since they do not need to tunnel through the barrier. (Even with this choice of barrier height 0.2% of the wave packet still has energy above the barrier. This is sufficiently small that we think it does not make a significant contribution to our result. At the present time I can not think of a better way to solve this problem. To only use energy below the barrier height for constructing the incoming wave-packet, it would be so wide that it would become impractical in this approach.) An addtional barrier height of 40eV has been added to a thin region just outside the left metal plate except where the parabolic tip is located, in order to further suppress contributions to the tunneling current that are not initiated from the tunneling tip. We will put one or two ions in the barrier directly between the tunneling tip and the location in the sample closest to the tip. We evolve the one-dimensional Gaussian wave packet initially sufficiently far from the barrier. We use 4096×128 grid points over a area of 96 Å$\times$ 24Å.

Δt is chosen to be $5\times10^{-4}eV^{-1}$, which is chosen to be sufficiently small so that the simulation will not go wrong. [14]

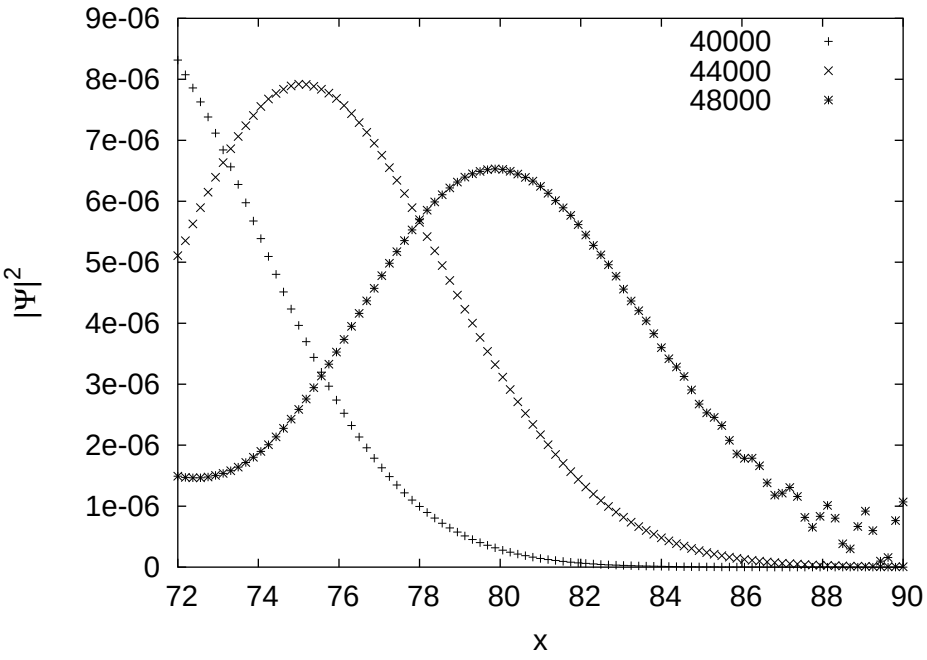

Fig. 8. $|\Psi|^2$ along the central line inside the sample at three time moments after certain time steps when there are no ions present inside the barrier. Note that the leftmost point corresponds to the sample surface.

3. Results

Fig. 8 and Fig. 9 show the results for the case when there is no charge in the barrier. Fig. 8 shows the evolution of $|\Psi|^2$ along the central line after certain time steps. We can see that at time $40000 \times \Delta t$, the tunneling wave packet has entered the sample, but the peak has not appear. At time $44000 \times \Delta t$, the peak has entered the sample. And after that the wave packet continues to propagate and becomes lower and wider. At time $48000 \times \Delta t$, the tunneling wave packet almost totally entered the sample. Fig. 9 shows $|\Psi|^2$ along the sample surface. We can see that the tunneling wave packet is focused by the tip. Its width is within 2Å. Fig. 10 shows $|\Psi|^2$ along the sample surface when we put a negative ion 2Å away from the sample surface along the center line. The charge of the ion is equal to the electron charge $-e < 0$. The potential in

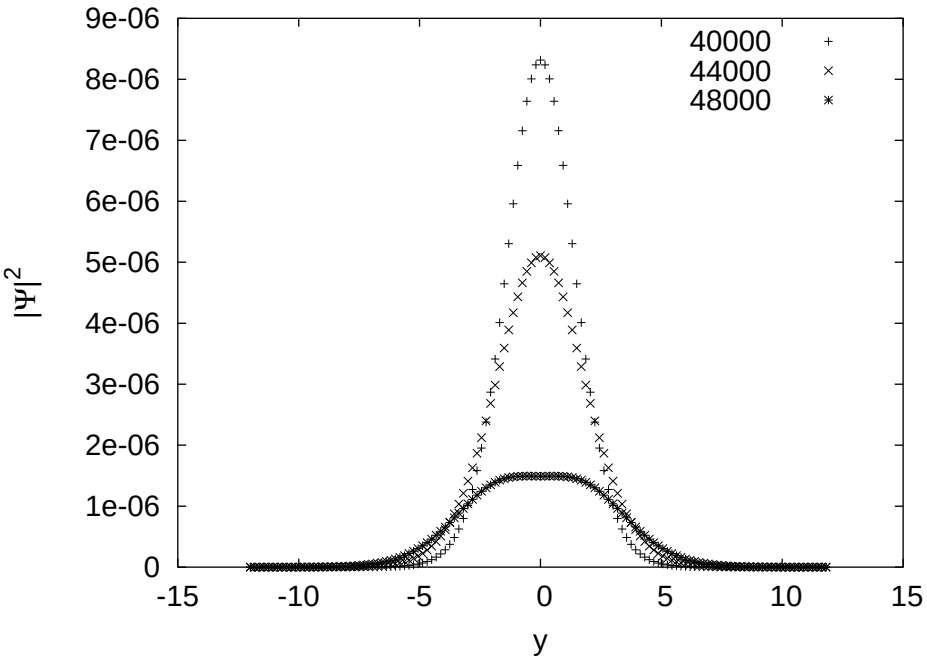

Fig. 9. $|\Psi|^2$ along the sample surface at the same three time moments as in Fig. 8 when there are no ions inside the barrier.

the barrier is the barrier height plus the bare Coulomb potential of the ion. A cutoff is introduced if the distance to the center of charge is within 0.7Å. We can clearly see that the wave packet is pushed away from the center by the negative ion in the barrier and splits into two parts. Figure 11 shows $|\Psi|^2$ along the sample surface when we put a positive ion 4Å away from the sample surface. The charge of the ion is $+e > 0$. Comparing to the case when there is no charge in the barrier, the tunneling wave packet is seen to become narrower, i.e., more focused. In Fig. 12, we show $|\Psi|^2$ along the sample surface when we put both a negative ion and a positive ion in the barrier. The positive ion is at 4Å from the sample surface, and the negative ion is at 2Å from the sample surface, both along the center line. (This charge arrangement is to more-or-less simulate the situation encountered by the tunneling electrons in the STM experiment on $Bi_2Sr_2CaCu_2O_8$.) We see that the tunneling wave packet has a

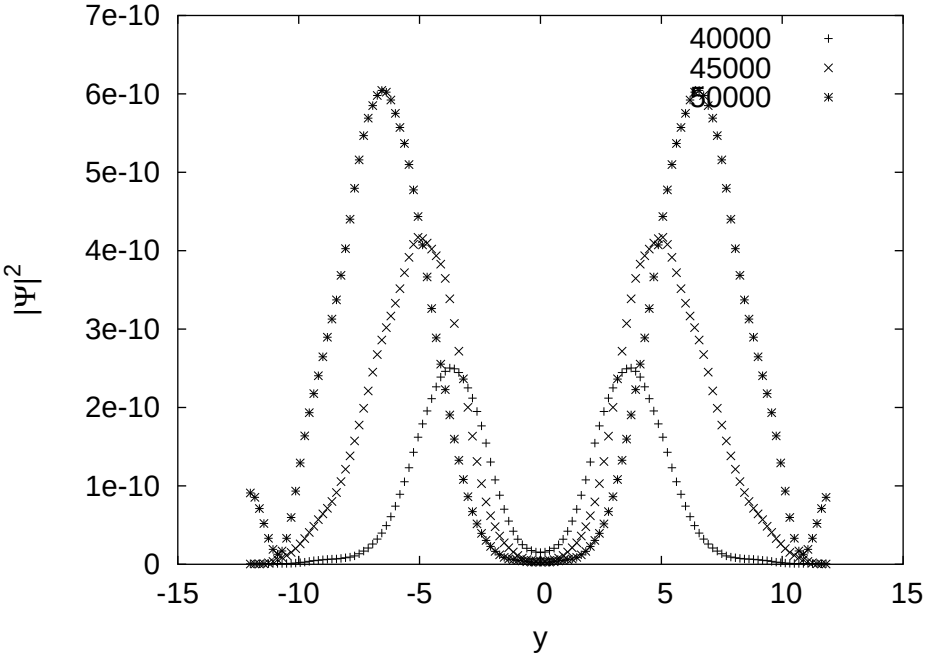

Fig. 10. $|\Psi|^2$ along the sample surface at three time moments after certain time steps when there is a negative ion with charge $-e$ inside the barrier.

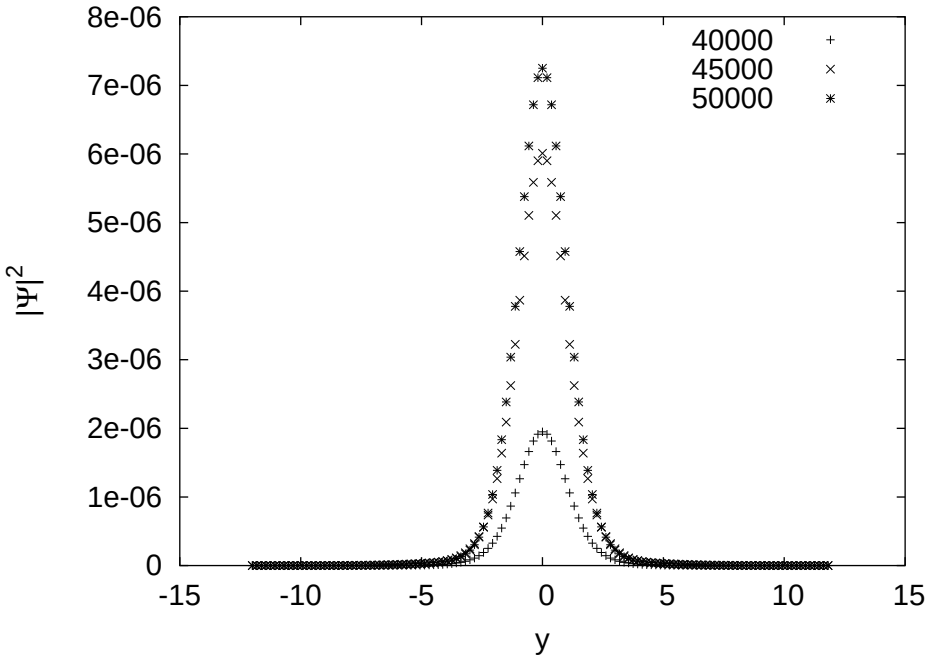

Fig. 11. $|\Psi|^2$ along the sample surface at three time moments after certain time steps when there is a positive ion with charge $+e$ in the barrier.

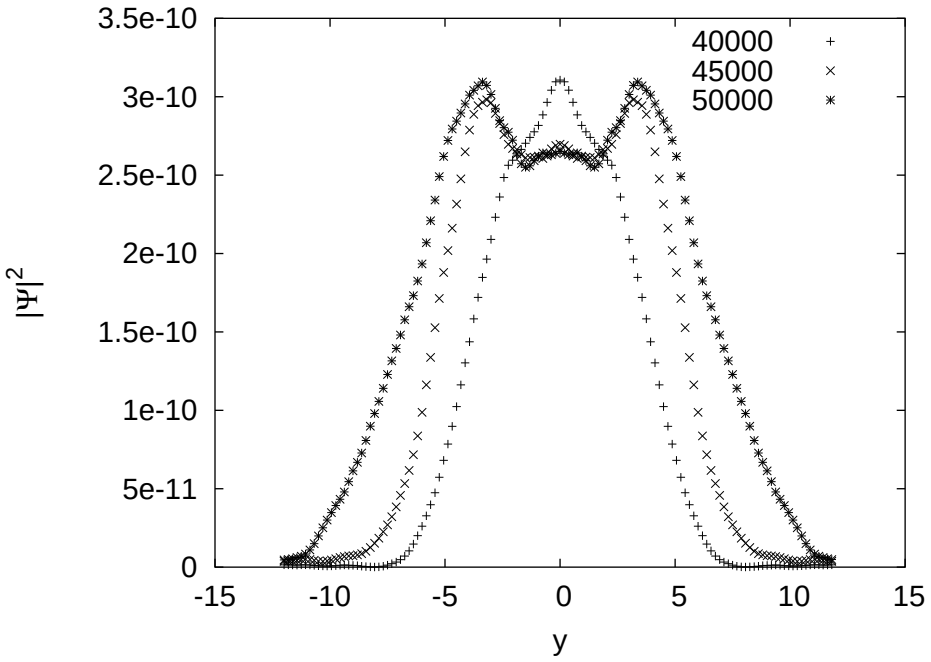

Fig. 12. $|\Psi|^2$ along the sample surface at three time moments after certain time steps when there is a $-e$ ion and a $+e$ ion in the barrier. The positions of the ions are given in the text.

focused component due to the positive ion and a split apart component due to the negative ion.

In BSCCO, the top layer is $Bi^{3+}O^{2-}$, the second layer is $Sr^{2+}O^{2-}$. Bi^{3+} ions in the first layer and O^{2-} ions in the second layer are straight above the Cu (or Zn) atoms in the superconducting layer. Bi^{3+} has positive charge and will focus the tunnel current. O^{2-} in the second layer has negative charge and will split apart the tunneling wave packet. In addition, the Sr^{2+} ions in the second layer have positive charges and they will tend to attract the tunneling wave packet. Thus we think that the spread of tunneling current along the CuO_2 plain will be even wider.

C. Conclusion

In summary, we have simulated localized tunneling process in STM by solving two-dimensional, time-dependent, Schrödinger equation. (We originally planned to solve three dimensional Schrödinger equation, but found that it would require too much computer time and memory to be possible.) We have shown that a negative ion in the barrier directly below the tunneling tip can deflect the tunneling electrons and prevent them from reaching a point in the target plane directly below the tunneling tip. This result shows that one must exercise caution when analyzing STM images obtained when the target plane of the tunneling process is not the top atomic layer of the sample, and there are other ionic layers between the tunneling tip and target layer, as is the case of cuprate superconductors such as $Bi_2Sr_2CaCu_2O_8$ investigated by Pan et al. [1]. This result also provides qualitative support for the blocking model proposed recently by Zhu et al. in Ref. [2] for explaining the resonant state image observed near a Zn impurity in the CuO_2 plane of $Bi_2Sr_2CaCu_2O_8$ using STM [1]. But it doesn't prevent some fine-tunning of the model, such as to allow part of the tunneling current to reach the Cu(Zn) site directly under the tip, because of the focusing effect of the Bi^{3+} ions. The calculation is done in two dimension so far. When sufficient computational resources become available, this method can be generalized to 3D. If a more accurate 3D potential could be obtained from another study, and much more powerful computers should become available, this study be extended to find the could exact tunneling path. Quantitative comparison with experiments might then be possible. Unfortunately, this is hard to reach at the present time.

CHAPTER IV

ON A FAMILY OF SURE SUCCESS QUANTUM SEARCH ALGORITHMS

A. Introduction

As the twentieth century was drawing close to to its end, a new field of application of quantum mechanics, quantum computing, emerged. Quantum computing brings together ideas from information theory, computer science, and quantum physics. It is an extension of classical computation, to the processing of quantum information, using quantum systems such as atoms, molecules or photons. The development of quantum information and computing theory proved to be fruitful. Among these are the quantum cryptography, quantum teleportation, quantum error correction, and quantum algorithms that outperform the corresponding classical algorithms. Physical implementation of quantum computation presents a profound experimental challenge. At present, there is not large scale quantum computation achieved in the laboratory and we do not know whether there will ever be one. But several team are working on small-scale systems and have obtain some exciting results. [15, 16]

Despite considerable efforts in the quantum computing community, the number of useful quantum algorithms which can significantly outperform the corresponding classical algorithms remains small. Most of these algorithms fall into two categories: Those for finding the period of a function and those for searching for an acceptable element in a large unsorted database. The primary contribution to the former is Shor's algorithm. [17] Based on quantum Fourier transformation, Shor's algorithm can factorize a large integer with a total cost $O(\log_2^3 N)$, [17] which represents a sub-exponential gain over the best classical algorithms, such as quadratic-sieve algorithm (with a total cost of $L(n)^{1+O(1)}$, where $L(n) = e^{\sqrt{\ln n \ln \ln n}}$), due to Pomerance. [18]

The main idea in the latter category is due to Grover. Grover's algorithm [19] solves the problem of searching for one acceptable element in a list of N unsorted elements. Classically, if the elements in the list are randomly distributed, we need to make $O(N)$ queries in order to find the desired elements, while Grover's quantum searching algorithm can perform the search with an efficiency of order $O(\sqrt{N})$. In general, Grover's original algorithm is not a sure-success one. There are several revisions of it to make it sure-success [20, 3]. In this article, I will extend the work of Hu [3].

B. Qubits

Quantum computing manipulates quantum information. The unit of quantum information is the quantum, or **qubit**. A qubit is a normalized vector $|\psi>=\alpha|0>+\beta|1>$, with $|0>$ denoteing the binary digit 0 and $|1>$ denoting 1, where α and β are complex numbers and satisfies $|\alpha|^2+|\beta|^2=1$. It can be physically implemented by a quantum two-level system like the two spin states of a spin 1/2 particle or the ground and an excited state of an atom. A measurement of a qubit in the state $|\psi>=\alpha|0>+\beta|1>$ yields the value 0 with probability $|\alpha|^2$ or the value 1 with probability $|\beta|^2$. If the answer 0 is observed, the state collapses to $|0>$; if the answer is 1, the state becomes $|1>$. A physical system of n qubits requires 2^n complex numbers to describe its state.

Qubits have some other features that we do not see in classical world. One of these features is entanglement. We say that a set of qubits is entangled if it can not be written as a tensor product of its parts. If a composite quantum system is entangled, it means that there are correlations between the subsystems. What we do with one part of the system will influence the other part. For example, consider two-qubit states $(|00>+|01>+|10>+|11>)/2$ and $(|01>+|10>)/\sqrt{2}$. The former can

be factored into $(|0> +|1>)/\sqrt{2} \otimes (|0> +|1>)/\sqrt{2}$. The latter cannot be factored and is thus entangled. When the two qubits of the latter are measured, they yield (01) or (10) with equal probability. But there is zero probability of getting (00) or (11). Another feature is that an unknown quantum state cannot be cloned. [21] This states that it is impossible to generate copies of a quantum state reliably, unless the state is already known.

To do computation, we need to do something to the qubits. The principle of quantum mechanics requires that the evolution of a quantum system must be unitary. So any transformation on qubits must be unitary.

C. Grover's Algorithm

In this section, we present the basic form of Grover's algorithm, which searches for one matching entry in an unsorted database with N entries.

Consider an unsorted database with N entries, which can be supplied by $n = \log_2 N$ qubits. Each state of the n-bit register represents an element in the database. Assume that there is a unique element x_0 that satisfies condition $f(x_0) = 1$, and for all other states $f(x) = 0$. This function f is called the "Oracle" operator. We assume that f can be evaluated in unit time. The task is to devise an algorithm which minimizes the number of evaluations of function f.

The procedure of Grover's algorithm is as follows:

1. Prepare a quantum register to the state $|\Psi_0> = N^{1/2} \sum_{x=1}^{N} |x>$. This is done by the following steps. First initialize the state to $|000...0>$. Then apply Walsh-Hadamard transformation to every qubit. A Walsh-Hadamard transformation changes the one-qubit state $|0>$ to $(|0> +|1>)/\sqrt{(2)}$, and the state $|1>$ to

$(|0> - |1>)/\sqrt{(2)}$.

2. Repeat $O(\sqrt{N})$ times the following two steps.

   i. Apply the "sign flipping" operator $\hat{F}_x = \hat{I} - 2|x_0><x_0|$ to the quantum register.

   ii. Apply the "inversion about the mean" operator $\hat{I}_s = \hat{I} - 2|s><s|$, where $|s> = 1/\sqrt{N}\sum_{i=1}^{N}|i>$, to the quantum register.

3. Perform the measurement on the quantum register. The quantum register will collapse to the target state with almost unity probability.

The number of iterations for step 2 has proved to be close to $\frac{\pi}{4}\sqrt{N}$ when N is large [22]. Since we can only perform integer number of iterations, we can not achieve zero failure except for $N = 4$.

D. Sure-Success Quantum Search Algorithm

Grover's original algorithm is not a sure-success algorithm and there is only one matching entry in the database. Several revisions have been proposed. A family of quantum algorithms $\{\mathcal{A}_n\}$ has been introduce by Hu [3] to find any one element with certainty in a set of acceptable elements which form a fraction f of the total number of elements in an unsorted database of size N. Here f is assumed to be known. The

"sign flipping" oracle operator $\hat{F}_x$ is generalized to

$$\hat{F}_\phi^{(a)} = \hat{I} - (e^{i\phi} + 1) \sum_{\nu \in a} |\nu >< \nu| \,, \tag{4.1}$$

where a denotes the set of acceptable elements in the database. This operator introduces the phase factor $-e^{i\phi}$ to each of the desired states. When $\phi = 0$ and a contains only one element, this operator reduces to the "sign-flipping" operator $\hat{F}_x$. The "inversion about the mean" operator is generalized to

$$\hat{O}_\theta = \sum_{i,j} [2\cos\theta/N - e^{i\theta}\delta_{i,j}]|i >< j| \,, \tag{4.2}$$

which reduces to the "inversion about the mean" operator if $\theta = 0$. Both $\hat{F}_\phi^{(a)}$ and $\hat{O}_\theta$ are unitary operators. The even member $\{\mathcal{A}_{2n}\}$ is defined as applying the unitary operator product $\hat{\Lambda} = \hat{O}_\theta^\dagger \hat{F}_\phi^{(a)\dagger} \hat{O}_\theta \hat{F}_\phi^{(a)}$ n times to the initial state $|\Psi_0>$, followed by the same measurement used in the Grover algorithm. The odd member $\{\mathcal{A}_{2n+1}\}$ is to apply the unitary operator product $\Gamma_n \equiv \hat{O}_\theta \hat{F}_\phi^{(a)} \Lambda^n$ to the state $|\Psi_0>$, before the same measurement is made. "Sure-success" of each of these algorithms is achieved by adjusting the two parameters θ and ϕ. In Ref. [3], $\mathcal{A}_1$, $\mathcal{A}_2$, $\mathcal{A}_4$ and $\mathcal{A}_6$ have been examined. Hu also made the following conjectures:

(i) For the even members, $\phi = 2\theta$ is always a valid solution, with θ depending on f, but not on N;

(ii) The f-range in which at least one θ value exists becomes ever larger if $\mathcal{A}_{2n}$ of ever larger n is considered, with the $n \to \infty$ limit being very likely the full range $0 \le f \le 1$;

(iii) In general the number of valid choices for θ increases to n deep inside the validity f-range for $\mathcal{A}_{2n}$.

In what follows, I will give general proof of these statements and extend the results to odd members. First we have

Lemma D.1.

$$\Lambda(\mu_0 - \nu_0 \hat{F}_\phi^{(a)\dagger})|\Psi_0>=(\mu_1 - \nu_1 \hat{F}_\phi^{(a)\dagger})|\Psi_0>, \tag{4.3}$$

where

$$\begin{pmatrix}\mu_1\\ \nu_1\end{pmatrix}=\begin{pmatrix}A_1 & -B_1^* e^{-2i\theta}\\ B_1 & -e^{-2i\theta}\end{pmatrix}\begin{pmatrix}\mu_0\\ \nu_0\end{pmatrix}, \tag{4.4}$$

$A_1 = |B_1|^2 - e^{2i\theta}$, *and* $B_1 = (2\cos\theta)e^{-i\theta}(1 - f - fe^{i\phi})$.

Lemma D.1 can be easily proved because we have $\Lambda|\Psi_0>\equiv \hat{O}_\theta^\dagger \hat{F}_\phi^{(a)\dagger}\hat{O}_\theta \hat{F}_\phi^{(a)}|\Psi_0>=[A_1 - B_1\hat{F}_\phi^{(a)\dagger}]|\Psi_0>$ and $\hat{O}_\theta^\dagger \hat{F}_\phi^{(a)\dagger}\hat{O}_\theta|\Psi_0>=e^{-2i\theta}(B_1^* - \hat{F}_\phi^{(a)\dagger})|\Psi_0>$.

Given Lemma D.1, we can prove the following theorem:

Theorem D.2. *(a): For the even members, suppose that* $\hat{\Lambda}^n|\Psi_0>=[A_n - B_n\hat{F}_\phi^{(a)\dagger}]|\Psi_0>$, *then* $\binom{A_n}{B_n}$ *satisfy:*

$$\begin{pmatrix}A_n\\ B_n\end{pmatrix}=f_n\begin{pmatrix}A_1\\ B_1\end{pmatrix}+g_n\begin{pmatrix}1\\ 0\end{pmatrix}, \tag{4.5}$$

where f_n *and* g_n *are real.*

(b): For the odd members, suppose that $\hat{O}_\theta\hat{F}_\phi^{(a)}\Lambda^n|\Psi_0>=[a_n - b_n\hat{F}_{-\phi}^{(a)\dagger}]|\Psi_0>$, *then* $\binom{a_n}{b_n}$ *satisfy*

$$\begin{pmatrix}a_n\\ b_n\end{pmatrix}=h_n\begin{pmatrix}a_0\\ b_0\end{pmatrix}+p_n\begin{pmatrix}0\\ e^{-i\theta}\end{pmatrix}, \tag{4.6}$$

where h_n *and* p_n *are real.*

Proof. First, we consider even members $\mathcal{A}_{2n}$. According to Eq. (4.4), we have the following recursive relationship for $\binom{A_n}{B_n}$: [3]

$$\begin{pmatrix}A_{n+1}\\ B_{n+1}\end{pmatrix}=\begin{pmatrix}A_1 & -B_1^* e^{-2i\theta}\\ B_1 & -e^{-2i\theta}\end{pmatrix}\begin{pmatrix}A_n\\ B_n\end{pmatrix}. \tag{4.7}$$

For n=1 in Eq. (4.5), we have $f_1 = 1$ and $g_1 = 0$. The statement in (a) is true. For n=2 , we have $f_2 = \left[|B_1|^2 - 2\cos 2\theta\right] = 4\cos\theta[(1 - f - f\cos\phi)^2 + f^2\sin\phi^2]$ and

$g_2 = -1$. They are both real, so the statement in (a) is also true. Suppose that for n=m Eq. (4.5) is true, we prove that for n=m+1, Eq. (4.5) is also true:

$$\begin{aligned}
\begin{pmatrix} A_{m+1} \\ B_{m+1} \end{pmatrix} &= \begin{pmatrix} A_1 & -B_1^* e^{-2i\theta} \\ B_1 & -e^{-2i\theta} \end{pmatrix} \begin{pmatrix} A_m \\ B_m \end{pmatrix} \\
&= \begin{pmatrix} A_1 & -B_1^* e^{-2i\theta} \\ B_1 & -e^{-2i\theta} \end{pmatrix} \left[f_m \begin{pmatrix} A_1 \\ B_1 \end{pmatrix} + g_m \begin{pmatrix} 1 \\ 0 \end{pmatrix} \right] \\
&= f_m \left[f_2 \begin{pmatrix} A_1 \\ B_1 \end{pmatrix} + g_2 \begin{pmatrix} 1 \\ 0 \end{pmatrix} \right] + g_m \begin{pmatrix} A_1 \\ B_1 \end{pmatrix} \\
&= (f_m f_2 + g_m) \begin{pmatrix} A_1 \\ B_1 \end{pmatrix} - f_m \begin{pmatrix} 1 \\ 0 \end{pmatrix} \\
&= f_{m+1} \begin{pmatrix} A_1 \\ B_1 \end{pmatrix} + g_{m+1} \begin{pmatrix} 1 \\ 0 \end{pmatrix}.
\end{aligned} \tag{4.8}$$

Hence Eq. (4.5) with real (f_n,g_n) holds for any n.

(b): For odd members, we substitute $\alpha = -\theta$ and $\beta = -\phi$ into Γ_n and transform it into $\Gamma_n = \Lambda^n_{\alpha,\beta} \hat{O}^\dagger_\alpha \hat{F}^{(a)\dagger}_\beta$. One has the identity:

$$\hat{O}^\dagger_\alpha \hat{F}^{(a)\dagger}_\beta |\Psi_0> = (a_0 - b_0 \hat{F}^{(a)\dagger}_\beta)|\Psi_0>, \tag{4.9}$$

where $a_0 = 2\cos\alpha(1 - f - fe^{-i\beta})$ and $b_0 = e^{-i\alpha}$.

For n=0, we have $h_0 = 1$ and $p_0 = 0$.

Suppose when n=m, the statement is true. We have

$$\begin{aligned}
\begin{pmatrix} a_{m+1} \\ b_{m+1} \end{pmatrix} &= [f_2 h_m - p_m] \begin{pmatrix} a_0 \\ b_0 \end{pmatrix} + h_m \begin{pmatrix} 0 \\ e^{i\alpha} \end{pmatrix} \\
&= h_{m+1} \begin{pmatrix} a_0 \\ b_0 \end{pmatrix} + p_{m+1} \begin{pmatrix} 0 \\ e^{i\alpha} \end{pmatrix}
\end{aligned} \tag{4.10}$$

.

Since f_2 is real, h_{m+1} and p_{m+1} are also real. Hence Eq. (4.6) with real (h_n,p_n) holds for any n. □

We thus have

Corollary D.3. *(a) $\phi = 2\theta$ is always a valid solution for even members.*

(b) $\phi = -2\theta$ is always a valid solution for odd members.

Proof. To ensure that an even member $\mathcal{A}_{2n}$ is a sure-success algorithm, one needs $A_n - B_n = 0$. The imaginary part of this condition can be written as $\mathtt{Im}(A_n - B_n) = f_n \mathtt{Im}(A_1 - B_1)$. So it can be satisfied with $\phi = 2\theta$. To ensure that an odd member $\mathcal{A}_{2n+1}$ is sure-success, one needs $a_n - b_n = 0$. Thus it requires $\mathtt{Im}[e^{i\theta}(a_n - b_n)] = h_n \mathtt{Im}[e^{i\theta}(a_0 - b_0)] = 0$. This can be satisfied with $\phi = -2\theta$. □

From the proof of Theorem D.2, we obtain the following recursion relations:

$$\begin{pmatrix} f_{n+1} \\ g_{n+1} \end{pmatrix} = \begin{pmatrix} f_2 & -1 \\ 1 & 0 \end{pmatrix} \begin{pmatrix} f_n \\ g_n \end{pmatrix}; \tag{4.11}$$

$$\begin{pmatrix} h_{n+1} \\ p_{n+1} \end{pmatrix} = \begin{pmatrix} f_2 & 1 \\ -1 & 0 \end{pmatrix} \begin{pmatrix} h_n \\ p_n \end{pmatrix}. \tag{4.12}$$

Solving Eq. (4.11) and (4.12), we obtain

$$f_n = \sin(n\gamma)/\sin\gamma, \tag{4.13}$$

$$h_n = \sin[(n+1)\gamma]/\sin\gamma, \tag{4.14}$$

where $f_2 = 2\cos\gamma$ and $\gamma \in [0, \pi]$.

So for even member $\mathcal{A}_{2n}$, solving $A_n - B_n = 0$ becomes solving the equations:

$$1 - 4f\cos^2\theta_{2n} = \frac{\sin[(n+1)\gamma]}{\sin(n\gamma)}, \tag{4.15a}$$

$$1 - 8f(1-f)\cos^4\theta_{2n} = \cos\gamma. \tag{4.15b}$$

For odd member $\mathcal{A}_{2n+1}$, solving $a_n - b_n = 0$ becomes solving the equations:

$$1 - 4f\cos^2\theta_{2n+1} = \frac{\sin(n\gamma)}{\sin[(n+1)\gamma]}, \tag{4.16a}$$

$$1 - 8f(1-f)\cos^4\theta_{2n+1} = \cos\gamma. \tag{4.16b}$$

The solutions of θ for these equations depend on f, but not on N. Solving these equations, we can obtain θ_n as a function of f. First we consider Eqs. (4.15). Let $f = \frac{1}{2}$, we have the

$$\cos^2\theta_{2n} = \frac{1 - \frac{\sin[(n+1)\gamma]}{\sin(n\gamma)}}{2}, \tag{4.17a}$$

$$\cos^2\theta_{2n} = \sqrt{\frac{1-\cos\gamma}{2}}. \tag{4.17b}$$

$\frac{\sin[(n+1)\gamma]}{\sin(n\gamma)}$ is monotonically decreasing function in every interval $(\frac{k\pi}{n}, \frac{(k+1)\pi}{n})$ of γ. Thus these equations have one solution in every interval $(\frac{k\pi}{n}, \frac{(k+1)\pi}{n})$ of γ. In total, there are n solutions. In Fig. 13, The curves for $\mu(\gamma) = \frac{1}{2}\left\{1 - \frac{\sin[(n+1)\gamma]}{\sin(n\gamma)}\right\}$ and $\mu(\gamma) = \sqrt{(1-\cos\gamma)/2}$ with $n = 4$ are shown. We can clearly see that there are 4 solutions. Setting $\theta = 0$ in Eqs. (4.15), we have found that there are two solutions for f in every interval $(\frac{k\pi}{n}, \frac{(k+1)\pi}{n})$ of γ. When n increases, the smallest f decreases. An illustration of $n = 4$ is shown in Fig. 14. This analysis confirms Hu's statements for even members. Solving Eqs. (4.16), we found that for odd members $\mathcal{A}_{2n+1}$, the f-range in which at least one θ exists becomes ever larger for ever larger n and always covers $f = 1$. In general, the number of valid choices for θ increases to $n + 1$ deep inside the validity f-range for $\mathcal{A}_{2n+1}$.

I have plotted θ as a function of f for even members $\mathcal{A}_8$, $\mathcal{A}_{10}$, and $\mathcal{A}_{12}$ in Figs. 15, 16, and 17. Figs. 18, 19, and 20 show θ as a function of f for odd members $\mathcal{A}_3$, $\mathcal{A}_5$, and $\mathcal{A}_7$.

E. Summary

In summary, I have studied an infinite family of sure-success quantum algorithms, which are introduced by Hu [3], for solving the generalized Grover search problem of finding any one element of a set of acceptable choices which constitute a fraction f

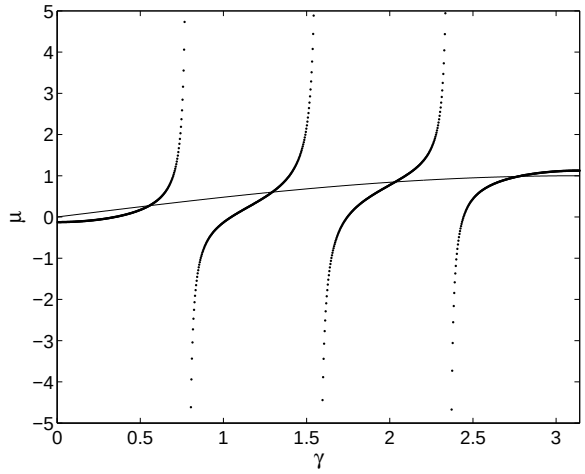

Fig. 13. Dotted line represents $\mu(\gamma) = \frac{1}{2}\left\{1 - \frac{\sin[(n+1)\gamma]}{\sin(n\gamma)}\right\}$; solid line represents $\mu(\gamma) = \sqrt{(1-\cos\gamma)/2}$. The y coordinates of the points where the dotted line intercepts the solid line are the solutions of Eqs. (4.15) for $\cos^2\theta$ when $f = 1/2$.

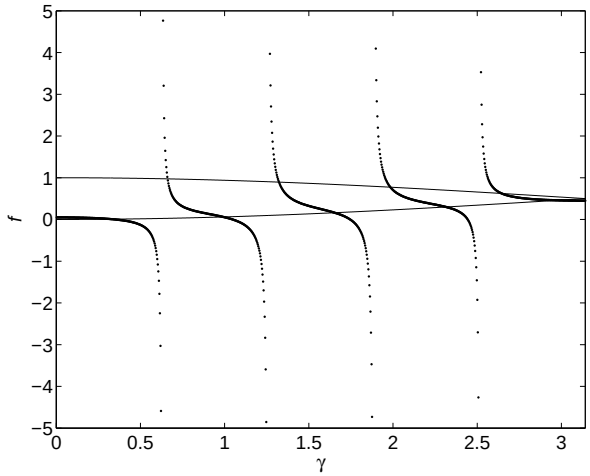

Fig. 14. Dotted line represents $f(\gamma) = \frac{1}{4}\left\{1 - \frac{\sin[(n+1)\gamma]}{\sin(n\gamma)}\right\}$; the two solid lines represent $f(\gamma) = \frac{1}{2}[1 \pm \sqrt{1 + (1-\cos\gamma)/2}]$. The y coordinates of the points where the dotted line intercepts the solid lines are the solutions of Eqs. (4.16) for f when $\theta = 0$.

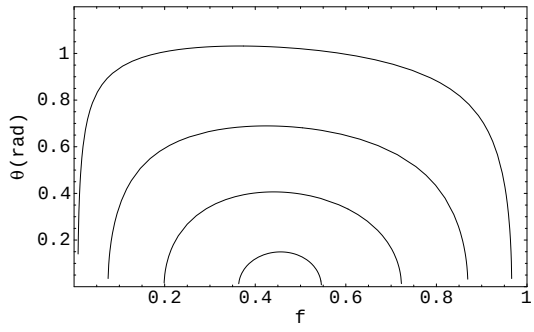

Fig. 15. Plotted is θ versus f for algorithm $\mathcal{A}_8$.

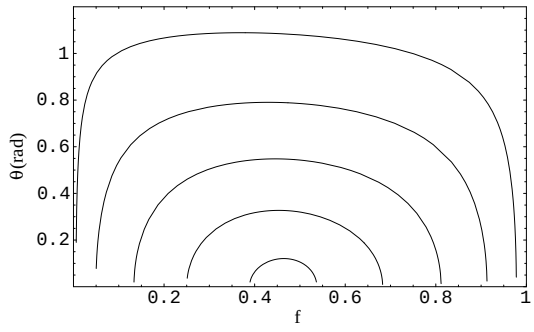

Fig. 16. Plotted is θ versus f for algorithm $\mathcal{A}_{10}$.

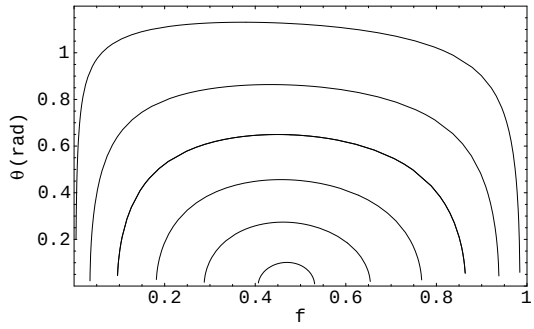

Fig. 17. Plotted is θ versus f for algorithm $\mathcal{A}_{12}$.

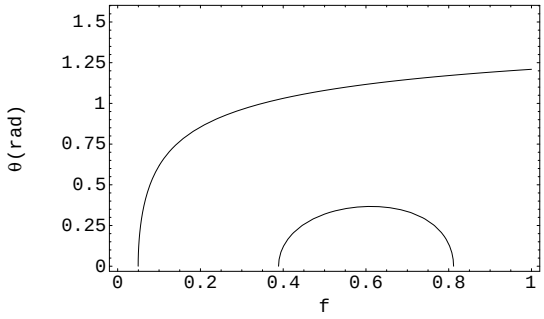

Fig. 18. Plotted is θ versus f for algorithm $\mathcal{A}_3$.

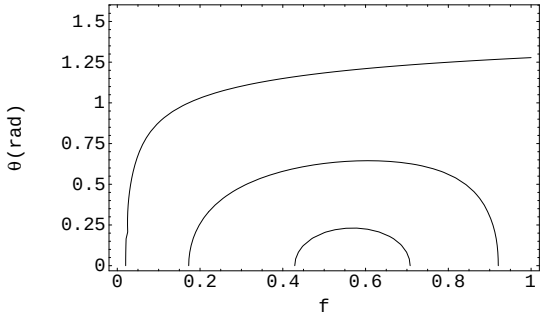

Fig. 19. Plotted is θ versus f for algorithm $\mathcal{A}_5$.

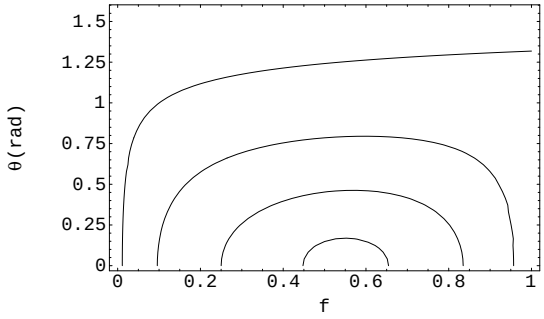

Fig. 20. Plotted is θ versus f for algorithm $\mathcal{A}_7$.

of all elements in an unsorted data base. I have proved that all the even members require $\phi = 2\theta$ and all the odd members require $\phi = -2\theta$. I have obtained explicit equations for finding θ for any given f and n. Using these equations I can show that all conjectures made by Hu in Ref. [3] are true, and have found corresponding statements for the odd members $\mathcal{A}_{2n+1}$ introduced by Hu.

CHAPTER V

HARTREE-FOCK SEARCH FOR DOUBLY-CHARGED ANTI-PHASE ISLAND IN AN EXTENDED HUBBARD MODEL

A. Introduction

The properties of strongly correlated electrons have drawn a lot of attention since the discovery of high-T_c superconductors. It is well established that the parent compounds of high-T_c superconductors, such as $La_{2-x}Ba_xCuO_{4-y}$, $YBa_2Cu_3O_{7-\delta}$, and $Bi_2Sr_2CaCu_2O_{8-\epsilon}$ are antiferromagnetic insulators. It has been found that in all of these compounds, as the hole-concentration x increases in the CuO_2 plane, the Néel temperature for the onset of antiferromagnetic order quickly drops to zero. As x is further increased, superconductivity was found to apear in a small range shortly after antiferromagnetism is destroyed. It is widely believed that the observed high-T_c superconductivity and antiferromagnetism in the cuprates are related.

It has been argued that this antiferromagnetism can be explained by a two-dimensional Hubbard model. [23] Hubbard model [24] is probably the simplest model of a strongly correlated electron system. It was originally proposed as a model of magnetic systems. The possibility that Hubbard model may exhibit superconductivity has been proposed for quite some time. For strong coupling, the ground state of Hubbard model at half filling is an antiferromagnetic insulating state. At very low doping, the very low concentration of doped holes are likely to form localized, immobile, singly-charged magnetic polarons (also known as spin-bags) [25]. Under Hartree-Fock approximation, Su [26] has shown that at intermediate U, the interaction between two spin polarons are attractive and two polarons lie on each other to form a doubly-charged spin bag. [26] Such a spin bag is deepest at its center and

so the two holes in it are likely to be in an s-wave orbital state. However, Hubbard model only considers on-site Coulomb repulsion and the Coulomb interaction between two charges on different sites are ignored. Since screening in two dimension is not as effective as in three dimension, this Coulomb interaction is likely unscreened until the separation between the two holes exceeds the mean distance between neighboring CuO_2 planes. This Coulomb repulsion between the two holes may convert the spin bag to d-wave. But once both charge carriers stay away from the center region in order to avoid getting too close to each other, antiferromagnetic phase might recover in that region to turn the doubly-charged spin-bag into a doubly-charged anti-phase island (DCHAPHI), which is the main idea of a new mechanism for high-T_c superconductivity proposed recently by Hu [4]. Hu proposed this new mechanism in order to understand two recent experiments: Xu et al. observed enhanced Nernst effect [27] and Iguchi et al. observed patched diamagnetism [28], both well above T_C in underdoped high-T_c superconductors. These two sets of experiments are briefly reviewed in the next paragraph.

Recently Xu et al. observed enhanced Nernst effect well above T_c in underdoped high-T_c cuprates. It occurs below an onset temperature T_ν, which first rises sharply at very low hole concentrations (x), reaching a peak at a hole concentration well below optimal doping, then decreases monotonically as x increases further. This effect is the observation of a voltage gradient transverse to both a temperature gradient applied along a slab-shaped sample and a magnetic field applied perpendicular to the sample. It is well known that enhanced Nernst effect can be observed below, at, and slightly above T_c of a low-T_c, type-II superconductor. It has been understood as due to the presence of vortex lines in the superconductor for the signal below T_c, and due to superconducting fluctuations for the signal at and slightly above T_c. A vortex line in a superconductor is also a magnetic flux tube containing a quantum of

magnetic flux, $\Phi_0 = hc/2e$, where h is the Planck constant, c is the speed of light, and e is the magnitude of the electron charge. The core of each vortex line has low-lying bound quasiparticle states with energies much below the superconducting gap. Thus there is extra entropy localized inside the vortex core. A positive temperature gradient along, say, the x direction then makes the vortex lines move toward $-x$. The concomitant motion of magnetic flux lines with the vortex lines then gives rise to a positive electric field along $-y$, if the applied magnetic field is in the z direction. Thus when Xu et al. observed enhanced Nernst effect well above T_c in underdoped high-T_c superconductors, they naturally attempt to associate it with vortices. But another recent experiment by Iguchi et al., using scanning superconducting quantum interference device (SQUID) microscopy, appears to have given evidence that this enhanced Nernst effect is not due to vortices. They observed vortices below T_c only, and patched diamagnetism well above T_c up to as high as 80K in $La_{2-x}Sr_xCuO_4$ with $x \approx 0.10$. Since fluctuation normally can give rise to enhanced Nernst effect only for a narrow temperature range above T_c, whereas T_ν can be as high as $\sim 100^\circ$ above T_c for some range of x, a new explanation of the observed enhanced Nernst effect in underdoped high T_c superconductors appears to be needed. (Fluctuation interpretation is also inconsistent with Iguchi et al.'s observation.)

Hu's proposal can qualitatively explain these observations, as well as the d-wave nature of pseudogap and pairing, and the x dependence of T_ν, T_c, etc. But it is only qualitative. We here perform a Hartree-Fock solution of the Hubbard model with the addition of quasi-long-range Coulomb interaction in order to seek confirmation of Hu's idea. (By "quasi-long range" we mean a screened Coulomb interaction with a screening length that is several lattice constants long.)

B. Hubbard Model

The two-dimensional, one-band, Hubbard-model Hamiltonian is given by:

$$\mathcal{H}_{\texttt{Hubbard}} = -t \sum_{<i,j>,\sigma}^{N} (c^{\dagger}_{i\sigma} c_{j\sigma} + c^{\dagger}_{j\sigma} c_{i\sigma}) + U \sum_{i=1}^{N} n_{i\uparrow} n_{i\downarrow} \,, \tag{5.1}$$

where $< i, j >$ denotes nearest neighbors, $c^{\dagger}_{i\sigma}$ ($c_{i\sigma}$) is the creation (annihilation) operator for spin $\sigma =\uparrow (\downarrow)$ at site i, and $n_{i\sigma} \equiv c^{\dagger}_{i\sigma} c_{i\sigma}$ with $\sigma =\uparrow$ and $\downarrow$ are the number operators. The first term in Eq. (5.1) describes nearest neighbor hopping. t is a the hopping matrix element. The second term in Eq. (5.1) describes an on-site Coulomb interaction, which works against double occupancy at any site. If U were infinite, at half filling every site would be occupied by one electron, with no hopping possible since it would cost $U = \infty$ for an electron to hop onto a site already occupied by one electron. As every spin configuration corresponds to an eigenstate of the interaction term, the system would be 2^N-fold degenerate, with N denotes the number of sites. While U is positive, the ground-state spin configuration is a unique antiferromagnetic state. Below is the argument why this is true for large and finite U. E. Lieb has given an rigorous proof for any positive U. [29] Consider any site at $\mathbf{x}_i$ and its four nearest-neighbor sites $\mathbf{x}_i \pm \mathbf{a}$ and $\mathbf{x}_i \pm \mathbf{b}$, where $\mathbf{a} = a\hat{x}$ and $\mathbf{b} = b\hat{y}$ are the lattice vectors along the x and y directions. If the spin at any one of these four neighboring site is different from the spin at $\mathbf{x}_i$, then the second-order-perturbation-theory correction to the eigen-energy, $\Delta E^{(2)}_n \equiv \sum_I \frac{<n|H'|I><I|H'|n>}{E^{(0)}_n - E^{(0)}_I}$, will lower the energy of this spin configuration. H' is the hopping part of the total Hamiltonian given in Eq. (5.1), which allows the electron at $\mathbf{x}_i$ to virtually hop onto this neighboring site to form a $(\uparrow\downarrow)$ pair, which is the intermediate state $|I >$, and then hop back. The energy denominator $E^{(0)}_n - E^{(0)}_I$ would be $-U$, since $E^{(0)}_n = 0$ due to no double occupancy at any site, and $E^{(0)}_I = U$ due to the presence of one $(\uparrow\downarrow)$ pair. Therefore ΔE_n is $-t^2/U$.

The total lowering in E_n would be the largest if the spin at every site is different from all of its neighboring sites. That is, the ground-state spin configuration must be an antiferromagnetic state.

Hubbard model has been under intense study using Hartree-Fock mean-field method. [26, 30, 31, 32]. In the absence of doping, the most stable configuration is the antiferromagnetic Néel state, for all values U/t. The value of the staggered magnetization increases smoothly as a function of U/t. Away from half filling, the Hartree-Fock solutions have at least two types, domain walls and spin-bags, for periodic systems. Domain walls are linear structures that separate different domains of the reference antiferromagnetic state. The extra charges are localized in the domain walls. Their width increases as the value of U/t decreases. Spin-bags are two-dimensionally localized structures. They are cigar or diamond shaped. In a spin-bag, the magnetization is reduced. As the doping increases, the spin-bag evolves into a large diamond-shaped object, the interior of which has the opposite staggered magnetization to the exterior. It can then also be viewed as a domain-wall ring enclosing an anti-phase island such as that in Fig. 21.

Hubbard model only includes on-site Coulomb interaction. Coulomb interaction between electrons on different sites is neglected. In the context of high-T_c study, usually U is large. When U is large, the on-site Coulomb interaction term is strong in comparison with the hopping term. In this case, off-site Coulomb interaction might be strong enough so that it should not be neglected. Therefore here we study an extended Hubbard Hamiltonian, which includes Coulomb repulsion between any pair of electrons on a two-dimensional square lattice. The Hamiltonian is as follows.

$$\mathcal{H} = \mathcal{H}_{\mathtt{H}ubbard} + V \sum_{i \neq j, \sigma, \sigma'}^{N} \frac{e^{-r_{ij}/r_0}}{r_{ij}} n_{i\sigma} n_{j\sigma'} \tag{5.2}$$

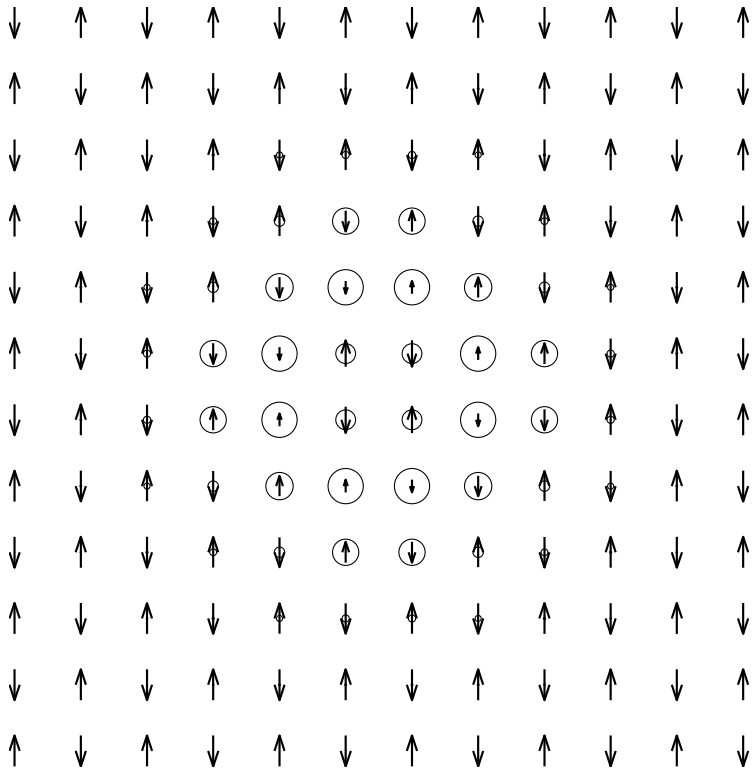

Fig. 21. Magnetic-polaron solution of the Hubbard model at $U/t = 8$, $n_h = 8$. Arrow denotes spin configuration (i.e., $< n_\uparrow > - < n_\downarrow >$. Circle denotes hole configuration (i.e., $1 - < n_\uparrow > - < n_\downarrow >$).

The second term on the right hand site of Eq. (5.2) describes the Coulomb interaction between electrons on different sites and r_0 is the screening length.

C. Hartree-Fock Approximation

We apply Hartree-Hock approximation to study ground state of this extended Hubbard Hamiltonian at zero temperature.

The on-site interaction term is linearized to

$$U\sum_i n_{i\uparrow}n_{i\downarrow} \to U\sum_i [< n_{i\uparrow} > n_{i\downarrow} + < n_{i\downarrow} > n_{i\uparrow} - < n_{i\uparrow} >< n_{i\downarrow} >] \tag{5.3}$$

The off-site Coulomb interaction is approximated by

$$\begin{aligned} &\frac{1}{2}V\sum_{i\neq j,\sigma,\sigma'} \frac{e^{-r_{ij}/r_0}}{r_{ij}} n_{i\sigma}n_{j\sigma'} \\ &\to \frac{1}{2}V\sum_{i\neq j,\sigma,\sigma'} \frac{e^{-r_{ij}/r_0}}{r_{ij}} [2n_{i\sigma} < n_{j\sigma'} > - < n_{i\sigma} >< n_{j\sigma'} >] \\ &- \frac{1}{2}V\sum_{i\neq j,\sigma} \frac{e^{-r_{ij}/r_0}}{r_{ij}} [2(c^\dagger_{i\sigma}c_{j\sigma}) < c^\dagger_{j\sigma}c_{i\sigma} > - < c^\dagger_{i\sigma}c_{j\sigma} >< c^\dagger_{j\sigma}c_{i\sigma} >] \end{aligned} \tag{5.4}$$

Then the Hamiltonian is approximated by

$$\mathcal{H} = \mathcal{H}_{HF} + E_0[n] \tag{5.5}$$

where

$$\begin{aligned} \mathcal{H}_{HF} = &- t\sum_{<i,j>\sigma} c^\dagger_{i\sigma}c_{j\sigma} + U\sum_{i,\sigma} n_{i\sigma} < n_{i-\sigma} > \\ &+ V\sum_{i\neq j,\sigma\sigma'} \frac{e^{-r_{ij}/r_0}}{r_{ij}} n_{i\sigma} < n_{j\sigma'} > -V\sum_{i\neq j,\sigma} \frac{e^{-r_{ij}/r_0}}{r_{ij}} c^\dagger_{i\sigma}c_{j\sigma} < c^\dagger_{j\sigma}c_{i\sigma} > \end{aligned} \tag{5.6}$$

and

$$E_0[n] = -U\sum_i < n_{i\uparrow} >< n_{i\downarrow} > -\frac{1}{2}V\sum_{i\neq j,\sigma\sigma'} < n_{i\sigma} >< n_{j\sigma'} > + \frac{1}{2}V\sum_{i\neq j,\sigma}\frac{e^{-r_{ij}/r_0}}{r_{ij}} < c^\dagger_{i\sigma}c_{j\sigma} >< c^\dagger_{j\sigma}c_{i\sigma} > \tag{5.7}$$

To diagonalize 5.6, a new set of fermion operators $c_{k\sigma}$ are introduced, so that we have

$$c_{i,\sigma} = \sum_k \phi_{ki,\sigma}c_{k,\sigma} \tag{5.8}$$

and they satisfy again fermion commutation relations.

Substituting Eq. (5.8) into Eq. (5.6), the Hartree-Fock Hamiltonian will take the diagonal form in $c_{k\sigma}$,

$$\mathcal{H}_{HF} = \sum_{k,\sigma}\epsilon_{k,\sigma}n_{k\sigma} \tag{5.9}$$

provided that ϕ_{ki} is chosen as eigenvectors of Eq. (5.6):

$$\mathcal{H}_{HF}\phi_{k\sigma} = \epsilon_{k\sigma}\phi_{k\sigma} \tag{5.10}$$

The ground state energy is optimized when $< n_{i\sigma} >$ satisfies the self consistency equations

$$< n_{i\sigma} > \;=\; \sum_k^{N/2}|\phi_{ki\sigma}|^2 < n_{k\sigma} >, \tag{5.11}$$

$$< c^\dagger_{i\sigma}c_{j\sigma} > \;=\; \sum_k^{N/2}\phi^*_{ki,\sigma}\phi_{kj,\sigma} < n_{k\sigma} > . \tag{5.12}$$

Because we study the system at zero temperature, the lowest N states are occupied and other states are empty. We have

$$n_{k\sigma} = \begin{cases} 1 & k \leq N/2 \\ 0 & \text{otherwise.} \end{cases}$$

The ground state of $\mathcal{H}_{HF}$ is given by

$$|\Phi_{HF}>=\prod_{k=1}^{N/2} c_{k\uparrow}\prod_{k=1}^{N/2} c_{k\downarrow}|\text{vac}> \tag{5.13}$$

and its wave function in real space is an N-state Slater-determinant:

$$\Phi_{HF}(R) = \mathtt{det}[\{\phi_{k\uparrow}(r_i)\},\{\phi_{k\downarrow}(r_j)\}], \tag{5.14}$$

where the rows of the determinant are composed of the set of N/2 lowest states of each spin. The total energy is given by

$$E_{HF} = 2\sum_{k}^{N/2}\epsilon_k + E_0[n]. \tag{5.15}$$

The single-determinant Hartree-Fock theory includes the exchange effects arising from the antisymmetry of the many-electron wave function, but neglects the electronic correlations caused by the electron-electron Coulomb repulsion. Correlation energies are a small fraction of the total energy, but they can be very important to the system we are studying, because we included Coulomb interaction between any two electrons on different sites and the anti-phase island proposed by Hu is a pairing mechanism. To include the correlation energies, one has to use more sophisticated techniques such as quantum Monte Carlo method. [33, 34, 35] But quantum Monte Carlo techniques rely on reasonable trial many-electron wave functions, which are often constructed using results obtained from Hartree-Fock calculations.

D. Results

The Hartree-Fock calculations are first carried out on a periodic 12×12 square lattice for a system with two holes in the supercell. The self-consistency conditions are satisfied by an iteration technique. For initial conditions of the iteration we used

three initial states: The trial charge and spin configurations are as those in Figs. 22-24. In all of these three configurations, the background is antiferromagnetic. Each site except for four sites at the center has one electron, with spin up or down. For the center four sites, each site has half an electron, *i.e.* there are altogether $4 \times (1 - \frac{1}{2}) = 2$ holes. In Fig. 22, an 2×2 antiphase-island is at the center, which has different phase from the background. In Fig. 23, an 2×2 spin-bag is at the center, which has the same phase as the background. In Fig. 24, each of the four sites at the center has $< s_z >= 0$. We set $t = 1$ for all our calculations.

Consider first the system at $U = 3.0$. When $V = 0$, the solution is shown in Fig. 25, which is the same for the three initial states used. This solution is the spin-bag solution obtained by Su in Ref. [26]. In the minimum energy configuration, two spin polarons with opposite spins lie on top of each other. This indicates that the interaction between them is attractive. The 2×2 sites at the center has the same antiferromagnetic phase as the background, only with weaker magnitude.

When we increase V to 0.1, we obtain the solution shown in Fig. 26. A small amount of excess electrons appears at the borders. We think these excess electrons are due to the Hartree-Fock approximation used. Hole densities at the sites around the center 2×2 sites become larger when compared with the $V = 0$ case. $|s_z|$'s at the center four sites still have the same phase as the background, but become smaller than those for the solution at $V = 0$. But when $V = 0.3$, we obtain the solution shown in Fig. 27. The excess electrons become larger at the borders. Hole densities at the eight sites around the center site are even larger than the $V = 0.1$ case due to the repulsion between the holes. The spin configuration at the center sites now has opposite staggered magnetization from other sites. This configuration clearly is a DCHAPHI. However it is different from the configuration conjectured by Hu. The largest hole accumulations are at the center four sites, whereas in Hu's

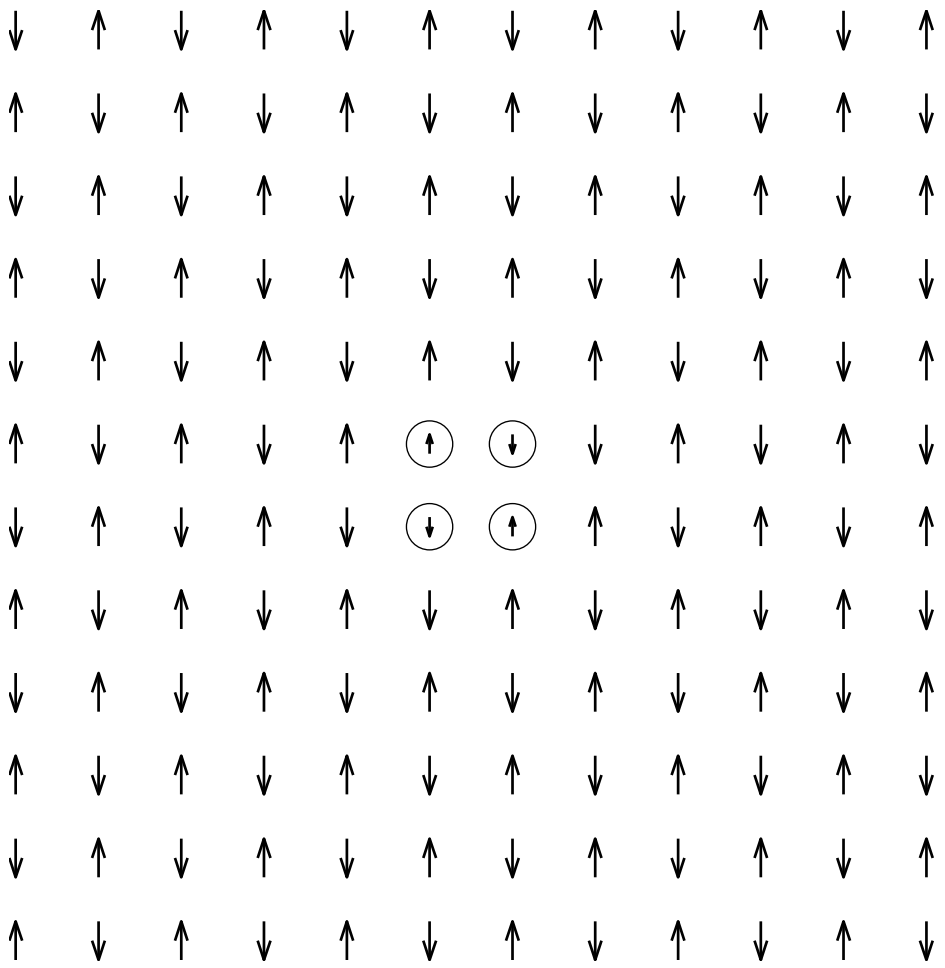

Fig. 22. The first initial state: A 2×2 antiphase-island in an antiferromagnetic background. At the center four sites the values of $n_\uparrow$ and $n_\downarrow$ are $\binom{0}{0.5}\binom{0.5}{0}$ $\binom{0.5}{0}\binom{0}{0.5}$.

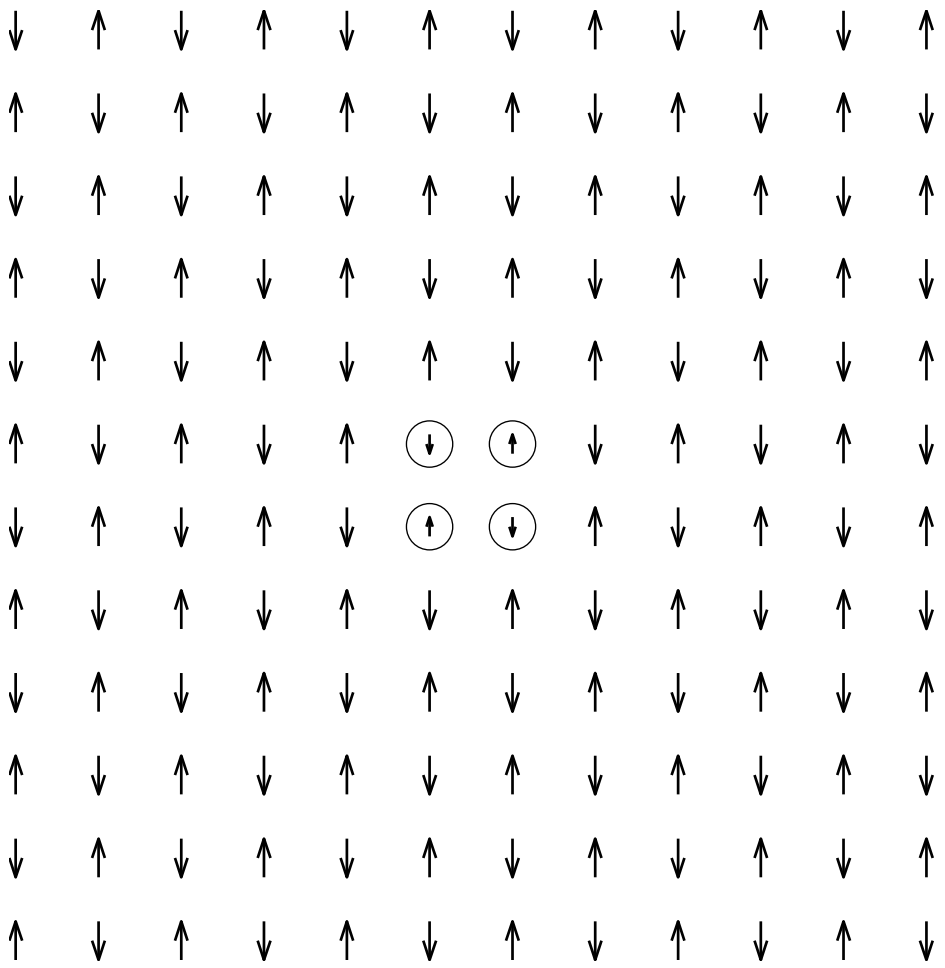

Fig. 23. The second initial state: Spin-bag in an antiferromagnetic background. At the center four sites the values of $n_\uparrow$ and $n_\downarrow$ are $\begin{pmatrix} 0.5 \\ 0 \end{pmatrix} \begin{pmatrix} 0 \\ 0.5 \end{pmatrix}$ $\begin{pmatrix} 0 \\ 0.5 \end{pmatrix} \begin{pmatrix} 0.5 \\ 0 \end{pmatrix}$

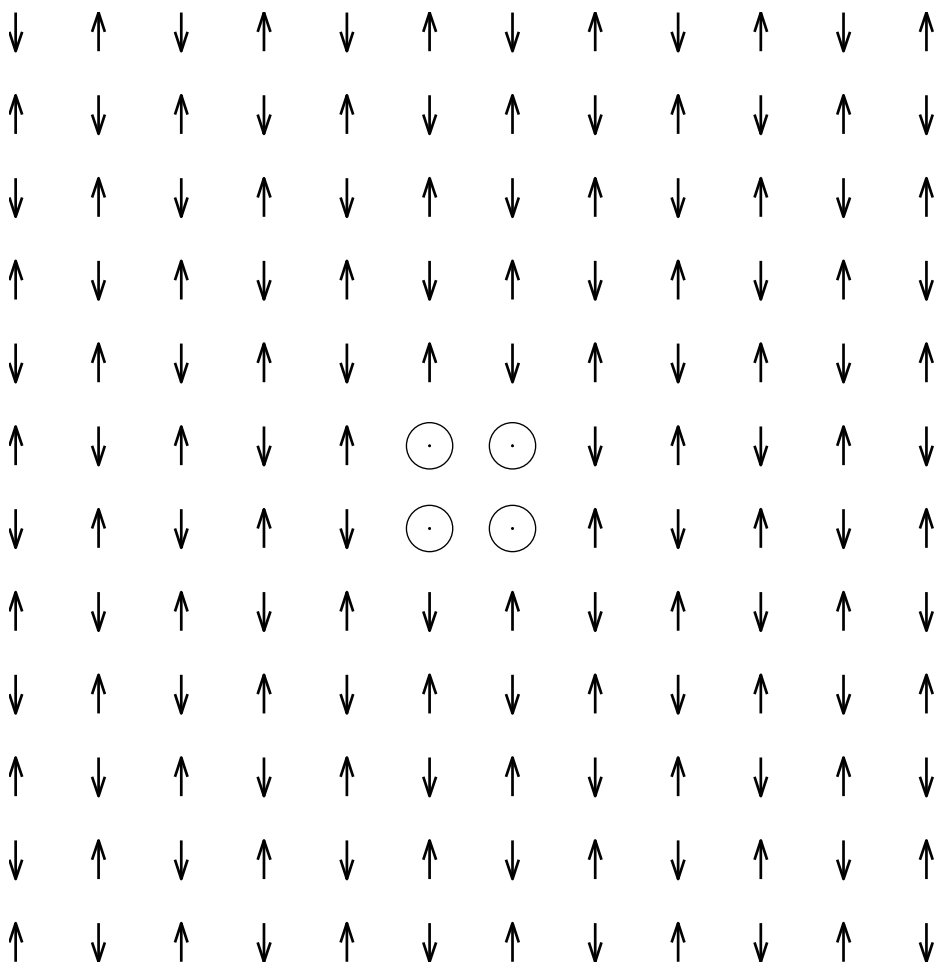

Fig. 24. The third initial state: At the center four sites the values of $n_\uparrow$ and $n_\downarrow$ are $\begin{pmatrix} 0.25 \\ 0.25 \end{pmatrix} \begin{pmatrix} 0.25 \\ 0.25 \end{pmatrix}$ $\begin{pmatrix} 0.25 \\ 0.25 \end{pmatrix} \begin{pmatrix} 0.25 \\ 0.25 \end{pmatrix}$.

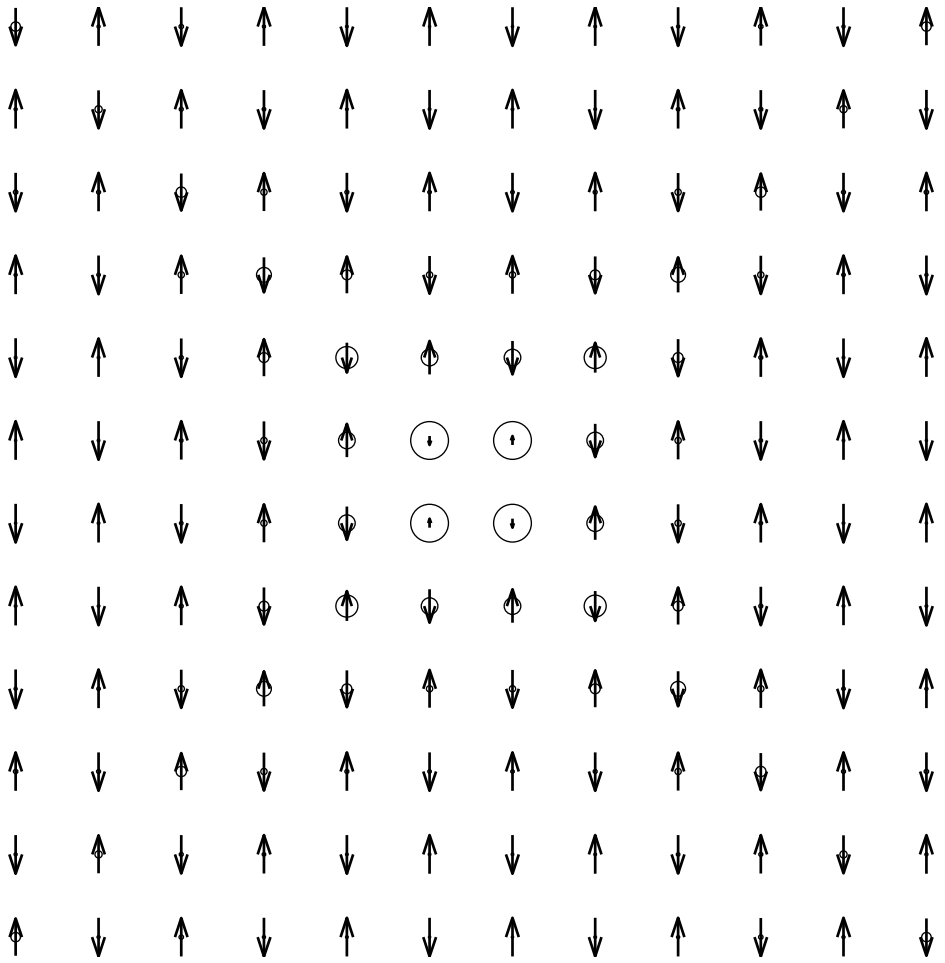

Fig. 25. Iterative Hartree-Fock solution of extended Hubbard model for $U = 3$ and $V = 0$ starting from all three initial states. Circle represents hole amount. Arrow represents spin.

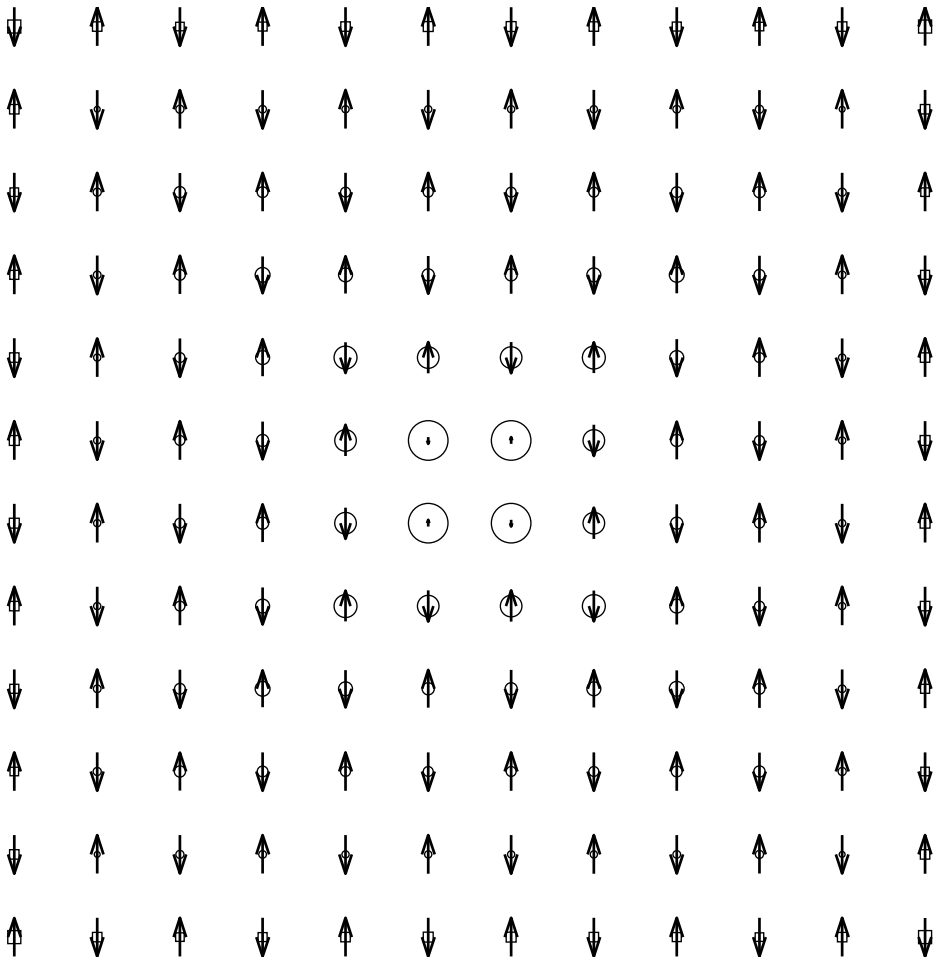

Fig. 26. Iterative Hartree-Fock solution of extended Hubbard model for $U = 3$ and $V = 0.1$ starting from all three initial states. Circle represents hole amount. Square denotes excess electron. Arrow represents spin.

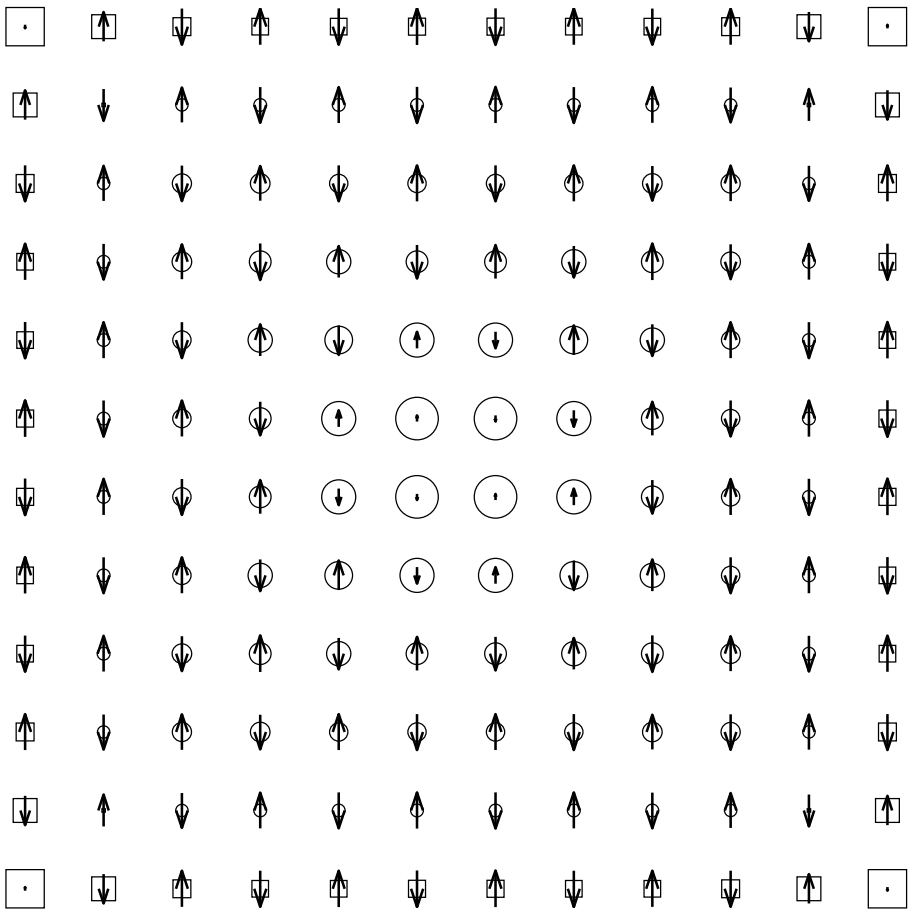

Fig. 27. Iterative Hartree-Fock solution of extended Hubbard model for $U = 3$ and $V = 0.3$ starting from all three initial states. Circle represents hole amount. Square denotes excess electron. At each of the four corners the solution gives 0.37 of an excess electron. Arrow represents spin.

conjecture they are mainly located at the eight sites just outside the center four sites. Another difference is that the spins at the eight sites around the center four sites are not zero, contrary to what Hu has conjectured. They have the same phase as the surrounding sites. However, we suspect that These differences might have resulted from the Hartree-Fock approximation used here, which does not take into account Coulomb correlation. Even studies going beyond the mean field theory may still not be able to settle this issue, since it is not clear how close they are to exact solutions which are not possible to obtain. If DCHAPHIs could be found experimentally, then the issue could be settled experimentally.

When we increase U to 8 with $V = 0$, we find that the system develops into two final states, shown in Figs. 28 and 29, depending on which initial state we choose to start our iteration. If we use Figs. 22 or 24 as the initial state, the final state is Fig. 29 with energy -68.59. This configuration is a DCHAPHI. If we start from Fig. 23, we obtain Fig. 28, which is a spin-bag and has a slightly higher energy -68.40. For the DCHAPHI solution, the eight sites around the center 2×2 sites have more holes then for the spin-bag solution. This situation continues when $V < 0.5$. In Fig. 30 and 31, we show the solution for $V = 0.3$. The energy is -15.98 for DCHAPHI and -15.80 for spin bag. We find that when $V = 0.5$, all the initial states will converge to a single state shown in Fig. 32, which is a DCHAPHI. When $U > 0.5$, the final state is always a DCHAPHI. The solution for $V = 0.8$ is shown in Fig. 33.

Results presented above have shown that at least in the mean field approximation a DCHAPHI can win over a spin bag as the lower energy configuration when there are two holes. It is then important to determine when there are more holes present, whether the system prefers to form many clearly separated DCHAPHIs (each possessing only two holes), or it will undergo some sort of phase separation, forming a big anti-phase island with many holes on its boundary, as has been obtained in

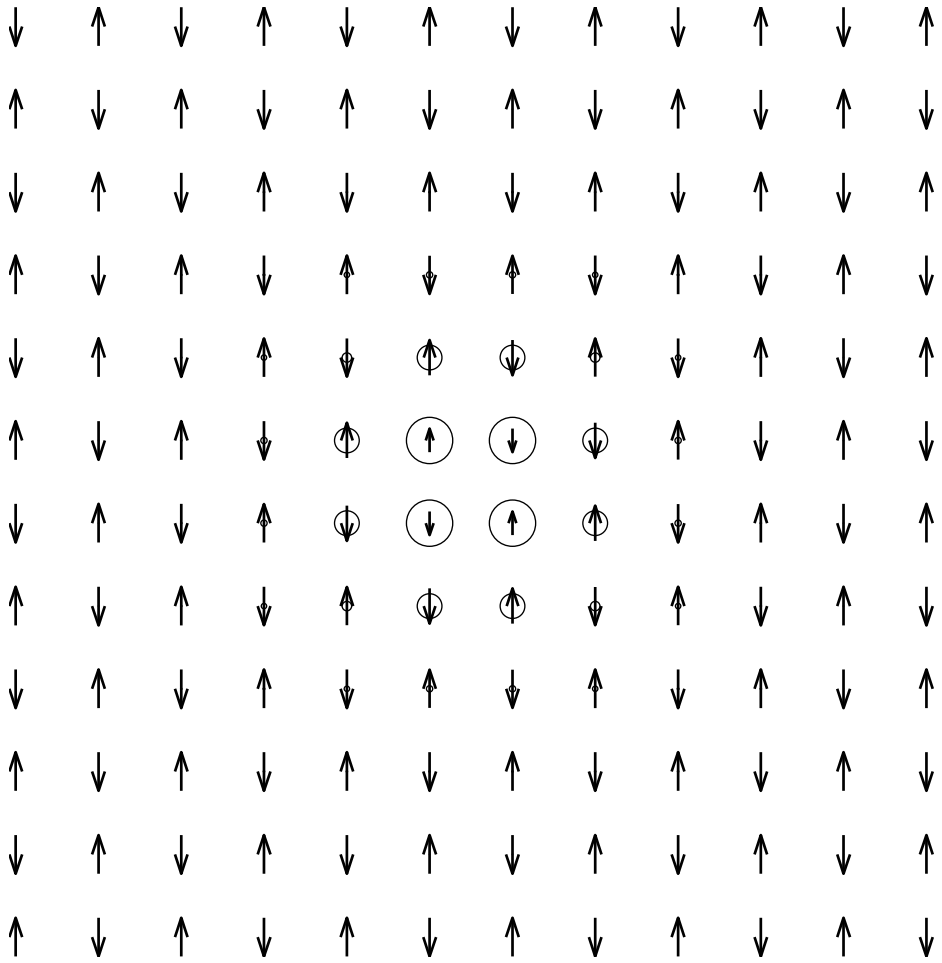

Fig. 28. Iterative Hartree-Fock solution of extended Hubbard model for $U = 8$ and $V = 0$ starting from the first and third initial states. Circle represents hole amount. Square denotes excess electron. Arrow represents spin.

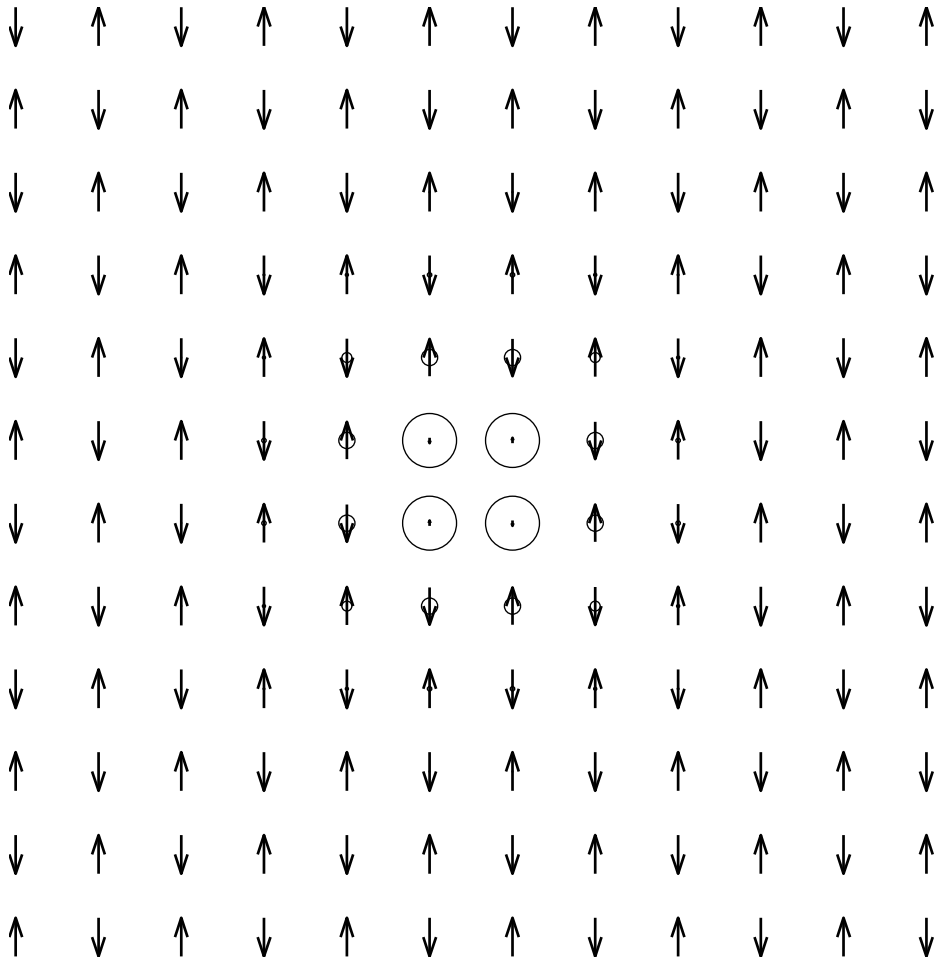

Fig. 29. Iterative Hartree-Fock solution of extended Hubbard model for $U = 8$ and $V = 0$ starting from the second initial state. Circle represents hole amount. Square denotes excess electron. Arrow represents spin.

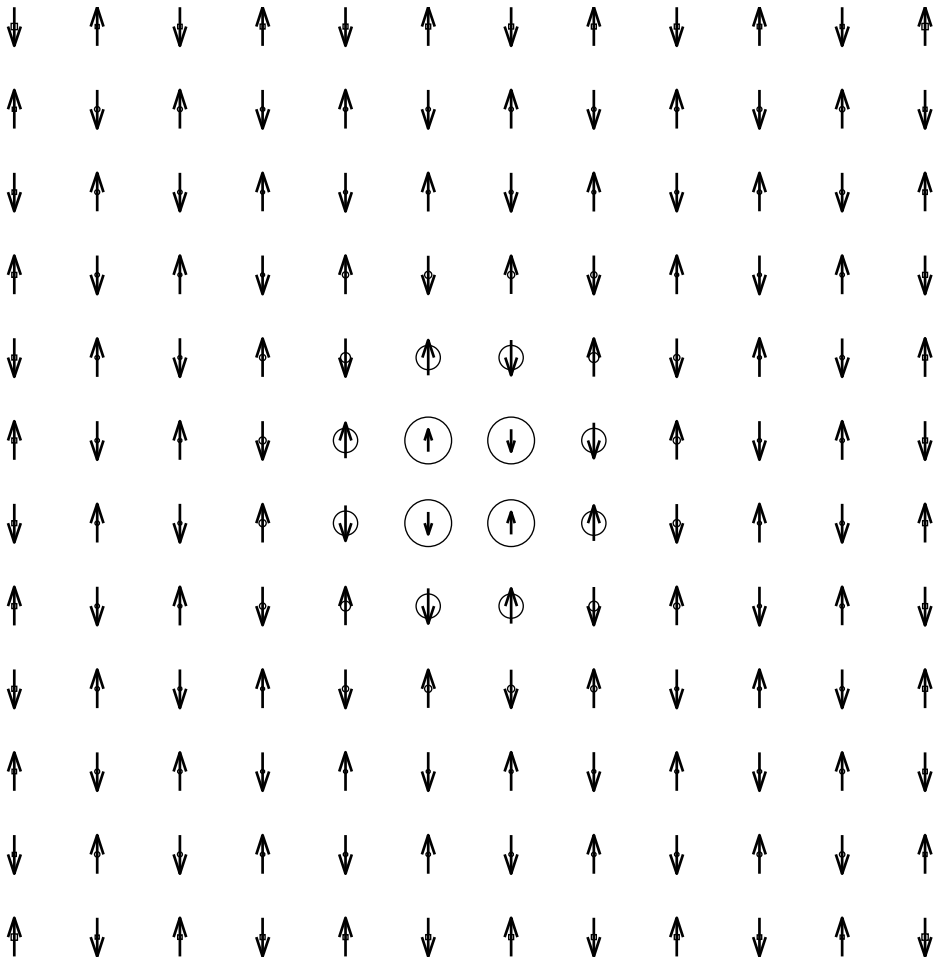

Fig. 30. Iterative Hartree-Fock solution of extended Hubbard model for $U = 8$ and $V = 0.3$ starting from the first and third initial states. Circle represents hole amount. Square denotes excess electron. Arrow represents spin.

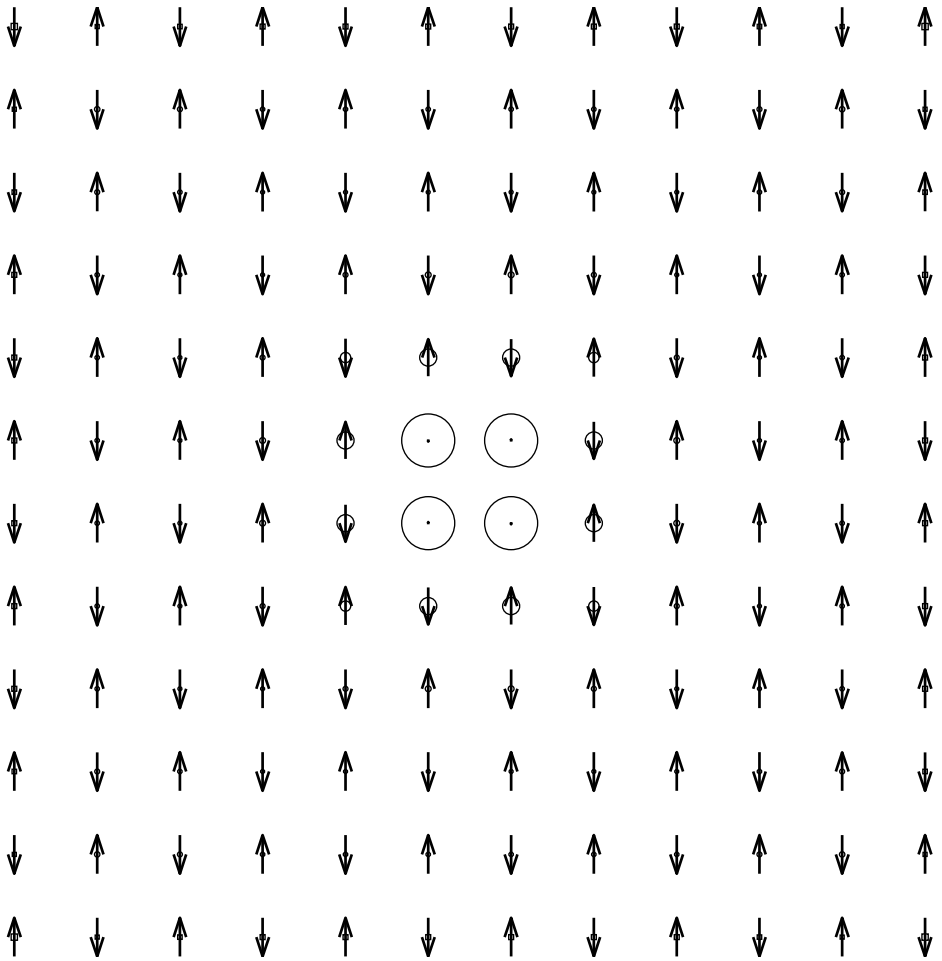

Fig. 31. Iterative Hartree-Fock solution of extended Hubbard model for $U = 8$ and $V = 0.3$ starting from the second initial state. Circle represents hole amount. Square denotes excess electron. Arrow represents spin.

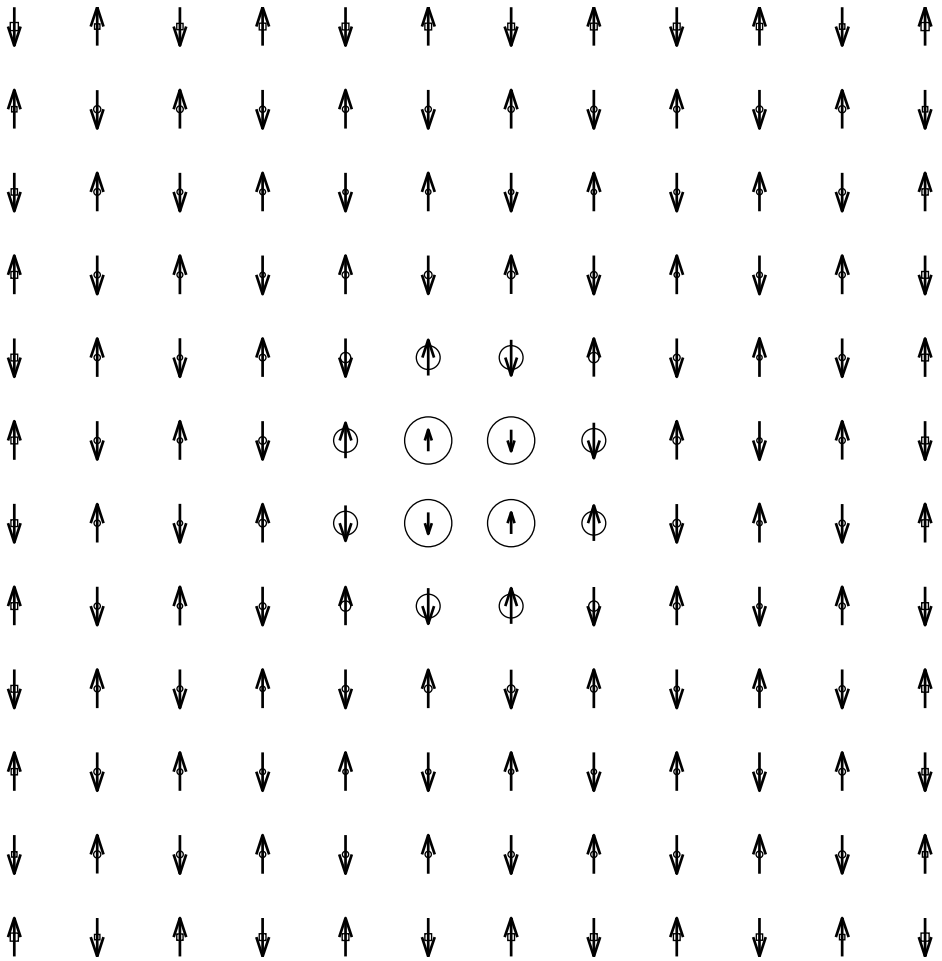

Fig. 32. Iterative Hartree-Fock solution of extended Hubbard model for $U = 8$ and $V = 0.5$ starting from all three initial states. Circle represents hole amount. Square denotes excess electron. Arrow represents spin.

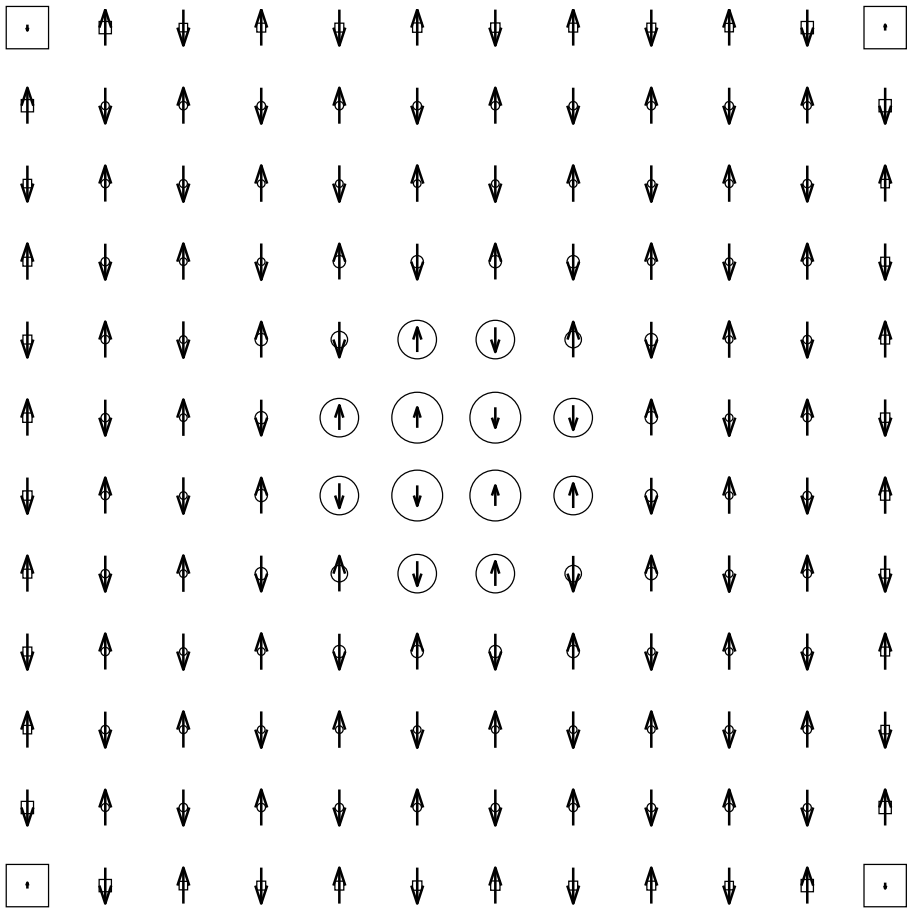

Fig. 33. Iterative Hartree-Fock solution of extended Hubbard model for $U = 8$ and $V = 0.8$ starting from all three initial states. Circle represents hole amount. Square denotes excess electron. Arrow represents spin.

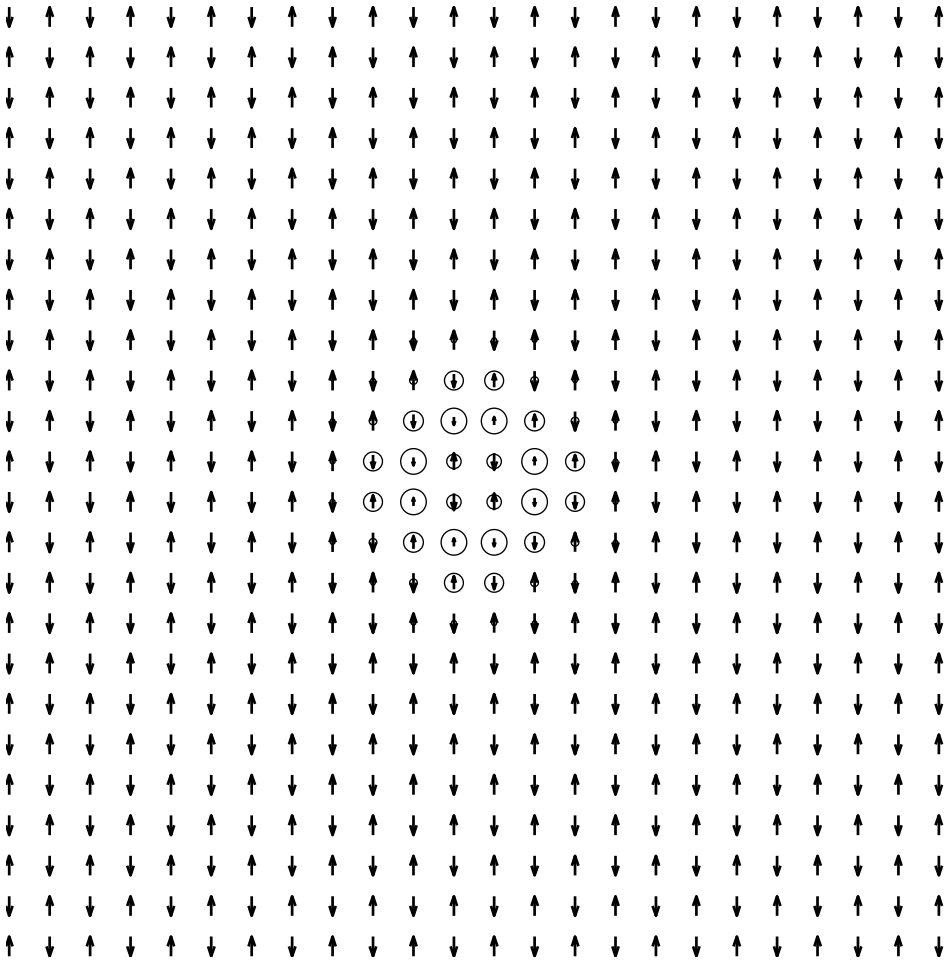

Fig. 34. 8-hole large-anti-phase-island solution for $U = 8$ and $V = 0$.

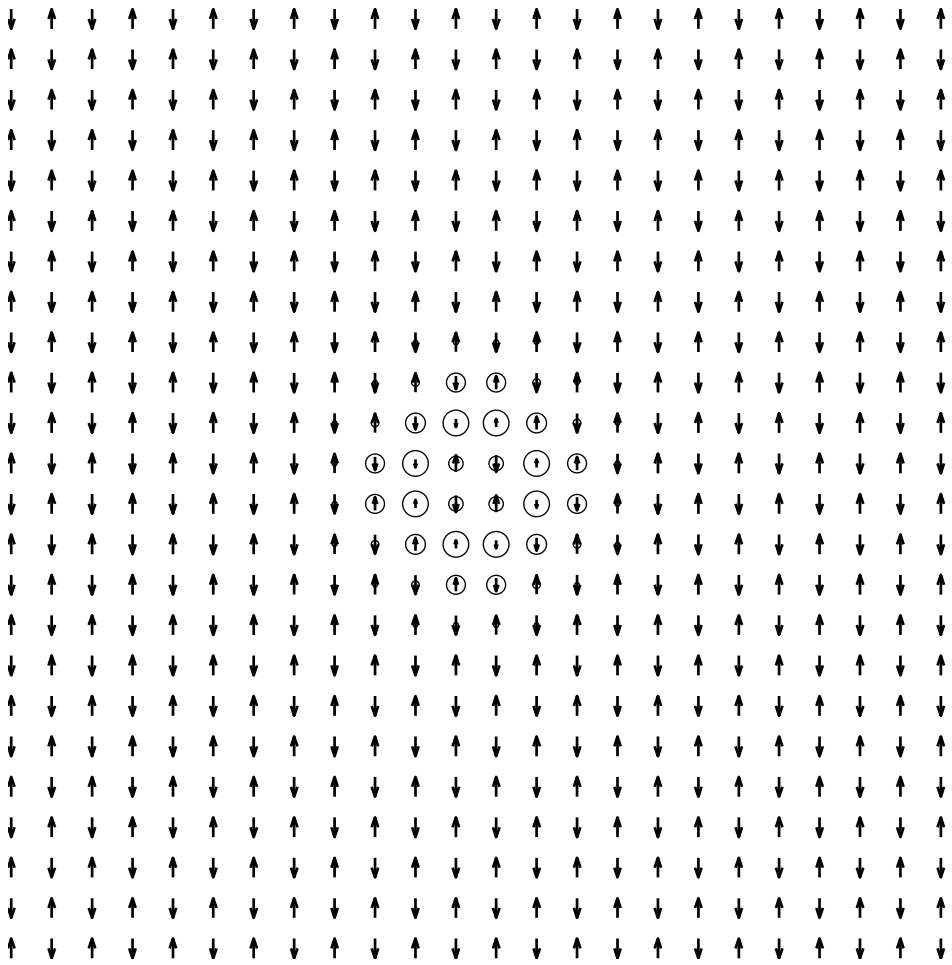

Fig. 35. 8-hole large-anti-phase-island solution for $U = 8$ with $V = 0.01$.

Ref. [30, 36] To address this issue, we obtained the following results within the mean field approximation.

For $U = 8$ and $V = 0$, we studies the extended Hubbard model in a 24×24 supercell with periodic boundary conditions. For the initial state we used a 2×2 anti-phase island with $n_\uparrow = n_\downarrow = 0$ at the eight boundary sites. The final state is shown in in Fig 34 and has an energy -276.6 which is lower than $-68.40 \times 4 = -273.6$ for four DCHAPHIs in four 12×12 supercells. Thus at $V = 0$ we find that phase separation is favored than separate DCHAPHIs.

When $V = 0.01$, we find that the energy for the eight-hole spin-bag solution shown in Fig. 35 becomes -244.13 and is now higher than $-65.8 \times 4 = -263.2$ for four separate DCHAPHIs. So even for very small positive V, separate DCHAPHIs become energetically favorable than the phase-separation solution.

E. Conclusion

In summary, we have studied a single-band extended Hubbard model, which includes quasi-long-range Coulomb interaction, using self-consistent Hartree-Fock theory. We find that for sufficiently large V/t, DCHAPHIs do become energetically favored localized objects in this system for moderate large values of U/t. When U/t is as large as 8, DCHAPHIs even exist at $V = 0$, and are energetically favored over doubly-charged spin-bags. Furthermore, We also find that for large enough U/t combined with small non-vanishing values of V/t, separate DCHAPHIs, each containing two holes, are energetically more favorable than a phase-separation solution where more than two holes collect on the domain-wall boundary of an anti-phase region. (We have tested it for the case of 8 holes.)

The DCHAPHI solutions we have found in this study has largest hole accumu-

lations at the center four sites, unlike Hu's conjecture which presumed that the two holes reside mostly on the eight boundary sites around the center four-site anti-phase island. So the relative orbital state of the two holes might still be s-wave. (Hu argued that it would be d wave.) As V increases, the percentage of hole concentration outside the center four sites increases. This is due to the Coulomb repulsion between the holes. The spins at those eight sites bordering the center four sites are not zero as conjectured by Hu, but have the same phase as the antiferromagnetic background. All these differences might be the result of the mean field approach used here.

Our study is based on Hartree-Fock approximation. The trial configurations has the upper-left/lower-right mirror symmetry and we maintained this symmetry in all our solutions in order to reduce numerical instability. Thus we can not rule out other Hartree-Fock solutions without this symmetry. The Hartree-Fock approximation only gives a qualitative understanding of the system under study. It is not a good method for studying the extended Hubbard model when U and V are large, because it underestimates quantum fluctuations and ignores correlation energy. Nevertheless, a Hartree-Fock solution can be a starting point for more sophisticated calculations, such as variational Monte Carlo method and quantum Monte Carlo method, which incorporate correlation effects more accurately.

REFERENCES

[1] S. H. Pan et al. Nature, 403, 746 (2000).

[2] J.-X. Zhu, C. S. Ting, and C.-R. Hu, Phys. Rev. B **62**, 6027 (2000).

[3] C.-R. Hu, Phys. Rev. A **66**, 042301 (2002).

[4] C.-R. Hu, Int. J. Mod. Phys. B. **17**, 3284 (2003).

[5] R. C. Dynes, Solid Stats Comm. **92**, 53 (1994); J. R. Schrieffer, *ibid.*, **92**, 129 (1994); D. J. Scalapino, Phys. Rep. **250**, 309 (1995); D. J. Van Harlingen, Rev. Mod. Phys. **67**, 515 (1995); C. C. Tsuei and J. R. Kirtley, *ibid.* **72**, 969 (2000).

[6] G. Preosti, H. Kim, and P. Muzikar, Phys. Rev. B **50**, 1259 (1994); R. Fehrenbacher and M.R. Norman, *ibid.* **50**, 3495 (1994); A.V. Balatsky, M.I. Salkola, and A. Rosengren, *ibid.* 51, 15 547 (1995); T. Xiang and J.M. Wheatley, *ibid.* 51, 11721 (1995); M.I. Salkola, A.V. Balatsky, and D.J. Scalapino, Phys. Rev. Lett. **77**, 1841 (1996); Y. Onishi et al., J. Phys. Soc.Jpn. 65, 675 (1996).

[7] A. Yazdani et al., Phys. Rev. Lett. **83**, 176 (1999); E. W. Hudson, S.H. Pan, A. K. Hupta, K.-W. Ng, and J.C. Davis, Science bf 285, 88 (1999); and Ref. [1].

[8] I. Martin, A. V. Balatsky, and J. Zaanen, Phys. Rev. Lett. **88**, 097003 (2002).

[9] F. C. Zhang and T. M. Rice, Phys. Rev. B **37**, 3759 (1988).

[10] A.V. Balasky, M.I. Salkola, and A. Rosengren, Phys. Rev. B **51**, 15547 (1995); M.I. Salkola, A.V. Balasky, and D.J. Scapapino, Phys. Rev. Lett. **77**, 1841 (1996); Y. Onishi, Y. Ohashi, Y. Shingaki, and K. Miyake, J. Phys. Soc. Jpn. **65**, 675 (1996); H. Tsuchiura, Y. Tanakan, M. Ogata, and S. Kashiwaya, J. Phys. Soc.

Jpn. **68**, 2510 (1999); J.-X. Zhu, T.K. Lee, C.S Ting and C.-R. Hu, Phys. Rev. B **61**, 8667 (2000).

[11] J. Tersoff, D.R. Hamann, Phys. Rev. Lett. **50**, 1998 (1983).

[12] J.Bardeen, Phys. Rev. Lett. **6**, 57 (1961).

[13] G. I. Márk et. al, Phys. Rev. B **62**, 2797 (1999).

[14] S. A. Chin and C. R. Chen, J. Chem. Phys.**114**, 7338 (2001).

[15] I. L. Chuang, N. Gershenfeld, and M. Kubinec, Phys. Rev. Lett. **80**, 3408 (1998).

[16] J. I. Cirac and P. Zoller, Nature, **404**, 579 (2000).

[17] P. W. Shor, SIAM J. Computing **26**, 1484 (1997).

[18] C. Pomerance, *Discrete Algorithms and Complexity*, Academic Press, New York, 119 (1987).

[19] L. K. Grover, Phys. Rev. Lett. **79**, 325 (1997).

[20] G. L. Long, Phys. Rev. A **64**, 022307 (2001).

[21] A. Steane, manuscript quant-ph/9708022 (1997).

[22] M. Boyer, G. Brassard, P. Høyer and A. Tapp, manuscript quant-ph/9605034 (1996).

[23] P. W. Anderson, Science **235**, 1196 (1987).

[24] J. Hubbard, Proc. R. Soc. London A **276**, 238 (1963).

[25] R. Schrieffer, X. G. Wen and S. C. Zhang, Phys. Rev. Lett. **60**, 944 (1988).

[26] W. P. Su, Phys. Rev. B **37**, 9904 (1988).

[27] Z. A. Xu et al., Nature **406**, 486 (2000).

[28] I. Iguchi, T. Yamaguchi, and A. Sugimoto, Nature **412**, 420 (2001).

[29] E. Lieb, Phys. Rev. Lett. **62**, 1201 (1989).

[30] J.A. Vergés, E. Louis, P.S. Lomdahl, F. Guinea, A.R. Bishop, Phys. Rev. B **43**, 6099 (1991).

[31] D. Poilblanc and T.M. Rice, Phys. Rev. B **39**, 9749 (1989).

[32] M. Inui and P.B. Littlewood, Phys. Rev. B **44**, 4415 (1991).

[33] W.M.C. Foulkes, L. Mitas, R.J. Reeds, and G. Rajagopal, Rev. Mod. Phys. **73**, 33 (2001).

[34] H.J.M. van Bemmel, D.F.B. ten Haaf, W. van Saarloos, J.M.J. van Leeuwen, and G. An, Phys. Rev. Lett. 72, 2442 (1994).

[35] J.B. Anderson, J. Chem. Phys. **63**, 1499 (1975).

[36] J. Zaanen and O. Hunnarsson, Phys. Rev. B. **40**, 7391 (1989).

APPENDIX A

MATLAB SUBROUTINE FOR ANALYZING RESONANT-STATE STM IMAGES

Find peaks around a impurity site. The peaks are assumed to be Gaussian. The quadratic fit code is taken from
http://www.cae.wisc.edu/ cs310/Matlab/surface_fit.m
written by Prof. Strikwerda.

```
clear;
clf;
%reading data
filename='C:\qwang\ZnImpurities\90414A05_-1.0mV.TXT'
m=DLMREAD(filename,'\t');
m1=m;   %m1 stores the original STM data
%end of reading data
[nx,ny]=size(m);   %size of the original data nx*ny
nofi=6;     %number of iterations
nop=15;     %number of peaks
ns0=2;      %number of points to include
 %in each dimension for fitting
xmin=20;ymin=20;
xmax=nx-20;ymax=ny-20;     %looking for peaks in this area
gray1(m1);
mtemp=zeros(nx,ny);
mx=zeros(nop,1);
```

```
my=zeros(nop,1);
        coe=zeros(nop,6);
for i=1:nop
    coe(i,1)=-30;   %set a_i1 negative and large
    mx(i,1)=(xmin+xmax)/2;
    my(i,1)=(ymin+ymax)/2;
end


for jjjj=1:nofi
    for jjj=1:nop
    m=m1;
    %subtracting contribution from other peaks
              for jj=1:nop
                  if(jj~=jjj)
                      for i=1:nx
                          for j=1:ny
                              cm=exp(coe(jj,1)+coe(jj,2)*i...
                               +coe(jj,3)*j+coe(jj,4)*i*i...
                               +coe(jj,5)*j*j+coe(jj,6)*i*j);
                              if (m(j,i)<cm)m(j,i)=1e-6;
                              else m(j,i)=m(j,i)-cm;
                              end
                          end
                      end
                  end
              end
```

```
                [y0,x0,temp]=max2(m) \find the highest point
            if(x0<xmax&x0>xmin&y0<ymax&y0>ymin)
%gaussian fit for each peak after
%subtracting contributions from other peaks
                ii=0;
                for i=-ns0:ns0
                    for j=-ns0:ns0
                        ii=ii+1;
                        xx(ii,1)=i+x0;
                        yy(ii,1)=j+y0;
                        zz(ii,1)=log(m(yy(ii,1),xx(ii,1)));
                    end
                end
                N=size(xx);
                for i = 1:N
    %constant term
                    A(i,1 ) = 1 ;
    %linear terms
                    A(i,2 ) = xx(i) ;
                    A(i,3 ) = yy(i) ;
    %quadratic terms
                    A(i,4 ) = xx(i)^2  ;
                    A(i,5  ) = yy(i)^2;
                    A(i,6  ) = xx(i) * yy(i) ;
                end
```

```
%Number of columns of least squares matrix.
M = length(A(1,:)) ;
%Get the QR decomposition of A.
%Q is an orthogonal matrix.
%R is upper triangular.
[Q,R] = qr(A) ;
%Invert the Q matrix.
%Q' is the transpose of Q, which is also
%the inverse since Q is orthogonal.
bb = Q'*zz;
%Get the top M by M matrix from R
RR = R( 1:M, : );
bb(1:M);
%Solve RR * c = bb
%Take only the top M entries of bb.
coef = RR\ bb(1:M);
%Compute the residual, method 1
%Compute the norm of the last N - M entries
%of bb. These are the equations that can not
%be solved.
r1 = norm( bb(M + 1: N ) );
%Compute the residual, method 2
```

```
%Find the norm of the vector of the difference
%of zz and the fit.
                r2 = norm( zz - A* coef );
%r1 should be equal to r2
                if(coef(4)<0&coef(5)<0...
                   &4*coef(4)*coef(5)-coef(6)*coef(6))
                    for i=1:nx
                        for j=1:ny
                            temp(j,i)=exp(coef(1)+coef(2)*i...
                               +coe(3)*j+coef(4)*i*i...
                               +coef(5)*j*j+coef(6)*i*j);
                        end
                    end
                    [y01,x01,temp1]=max2(mtemp);
                    if(y01<ymax&x01<xmax&y01>ymin&x01>xmin...
                       &abs(x01-x0)<=2&abs(y01-y0)<=2
                       &abs(temp1-temp)<(temp/2))
                        my0(jjj,1)=y01;
                        mx0(jjj,1)=x01;
                        for i=1:6
                            coe(jjj,i)=coef(i);
                        end
                    else coe(jjj,1)=-30;
                        for i=2:6
```

```
                            coe(jjj,i)=0;
                        end
                    end
                else  coe(jjj,1)=-30;
                    for i=2:6
                        coe(jjj,i)=0;
                    end
                end
            else coe(jjj,1)=-30;
                for i=2:6
                    coe(jjj,i)=0;
                end
            end
        end
    end
m=zeros(nx,ny);
    for jj=1:nop
        for i=1:nx
            for j=1:ny
                cm=exp(coe(jj,1)+coe(jj,2)*i+coe(jj,3)*j...
                  +coe(jj,4)*i*i+coe(jj,5)*j*j+coe(jj,6)*i*j);
                m(j,i)=m(j,i)+cm;
            end
```

```
            end
            if(coe(jj,2)==0)
                intensity(jj)=0;
            else
                int=2.0*3.1415927...
                /sqrt(4*coe(jj,4)*coe(jj,5)-coe(jj,6)*coe(jj,6))...
                *exp((coe(jj,5)*coe(jj,2)*coe(jj,2)...
                -coe(jj,6)*coe(jj,2)*coe(jj,3)...
                +coe(jj,4)*coe(jj,3)*coe(jj,3))...
                /(coe(jj,6)*coe(jj,6)-4*coe(jj,4)...
                *coe(jj,5))+coe(jj,1));
               intensity(jj)=int;
            end
        end
%output fitted data and draw a density plot of fitted data
newfilename=strcat(filename,'fit');
dlmwrite(newfilename,m,'\t');
figure;
gray1(m);
%output parameters of all peaks
coe   %output coeffients of all peaks
mx0   %output x coordinates of all peaks
my0   %output y coordinates of all peaks
intensity \ouput intensities
```

APPENDIX B

CODE FOR SOLVING HARTREE-FOCK EQUATION FOR EXTEND HUBBARD MODEL

```
#include <stdio.h>
#include <math.h>
#define t 1.0
int main(void){
    char jobz='V'; //compute eigenvalues and eigenvectors
    char uplo='L'; //Upper triangle of A is stored
    int size=12;
    int N1=size*size;
    int N=N1;
    int Lea=N;
    int i,j,l,k,kk;
    int row;
    int col;
    double wup[N1],wdown[N1]; //store eigenvalues
    double c;
    int lwork=3*N-1;
    int info;
    double work[lwork];
    double Hup[N1][N1]; //Hamiltonian matrix, store eigenvectors
    double niup[N1],nidown[N1];
    double up=1.0;
```

```
double E;
double r;
double kappa=4.0;
double temp,temp1,temp2;
FILE *spin,*spino;
FILE *density,*densityo,*H;
double psiup[N1][N1],psidown[N1][N1];
int nofi,nofh;
double U,V;
double nofs,nofd;
FILE *input;
input=fopen("input","r");
fscanf(input,"%d",&nofi);
fscanf(input,"%d",&nofh);
fscanf(input,"%lf",&U);
fscanf(input,"%lf",&V);
printf("%d\t%d\t%lf\t%lf\n",nofi,nofh,U,V);
fclose(input);
spin=fopen("spin.data","w");
spino=fopen("spino.data","w");
densityo=fopen("densityo.data","w");
density=fopen("density.data","w");
H=fopen("wavef.data","w");
for (i=0;i<size;i++){
    for (j=0;j<size;j++){
        if (fmod(i+j,2)==0){
```

```
            niup[i*size+j]=up;
                nidown[i*size+j]=1-up;
        }
        else {
            niup[i*size+j]=1-up;
            nidown[i*size+j]=up;
        }
    }
}
//
//anti-phase island
for (i=size/2-1;i≤size/2;i++){
    for (j=size/2-1;j≤size/2;j++){
        /*if(k<3){
        niup[i*size+j]=temp*rand()/(RAND_MAX+1.0);
        temp-=niup[i*size+j];
        k=k+1;
        nidown[i*size+size-1-j]=niup[i*size+j];
        }
        else {
        niup[i*size+j]=temp;
        nidown[i*size+size-1-j]=temp;
        }
        */
        niup[i*size+j]/=2.0;
        nidown[i*size+j]/=2.0;
```

```
            temp=niup[i*size+j];
            niup[i*size+j]=nidown[i*size+j];
            nidown[i*size+j]=temp;
            //niup[i*size+j]=0.25;
            //nidown[i*size+j]=0.25;
            //if(i==size/2-1){
            //niup[i*size+j]=0;
            //nidown[i*size+j]=0;
            //}
        }
    }
    for (k=0;k<(N-nofh)/2;k++){
        for(j=0;j<N;j++){
            psiup[k][i]=0;
            psidown[k][i]=0;
        }
    }
    for(i=0;i<N;i++){
        fprintf(spino,"%f",niup[i]-nidown[i]);
        fprintf(densityo,"%f",1-niup[i]-nidown[i]);
        if(fmod(i+1,size)==0) {
              fprintf(spino,"\n");
         fprintf(densityo,"\n");
          }
        else {
              fprintf(spino,"\t");
```

```
        fprintf(densityo,"\t");
        }
}
//
for (l=0;l<nofi;l++){
      printf("%d\n",l);
      for(i=0;i<N;i++){
            for(j=0;j<N;j++){
                  Hup[i][j]=0;
            }
      }
      /*diagonal metrix elements and hopping term of Hup*/
          for (i=0;i<N;i++){
                Hup[i][i]=U*nidown[i];
                for(j=0;j<N;j++){
                 temp=0;
                 if(V≠0){
                 for(k=-4;k≤4;k++){
                       for(kk=-4;kk≤4;kk++){
                             if (k==0&&kk==0&&i==j);
                                   else{
                             row=j/size+k*size-i/size;
                             col=j%size+kk*size-i%size;
                       r=sqrt((double)(row*row+col*col));
                             temp+=exp(-r/kappa)/r;
                             }
```

```
        }
    }
    }
    Hup[i][i]+=V*(niup[j]+nidown[j])*temp;
    temp=0;
    if(V!=0&&i==j){
    for(k=-4;k<=4;k++){
        for(kk=-4;kk<=4;kk++){
                                    if(k==0&&kk==0);
            else{
              row=k*size;
              col=kk*size;
              r=sqrt((double)row*row+col*col);
              temp+=exp(-r/kappa)/r;
              }
        }
    }
    Hup[i][i]-=V*niup[i]*temp;
    }
}


   if((i+1)%size==0)
        Hup[i][i-size+1]=-t;
      else Hup[i][i+1]=-t;
   if(i+size≥N)
```

```
                    Hup[i][i%size]=-t;
        else Hup[i][i+size]=-t;
            if(i%size==0)
                Hup[i][i+size-1]=-t;
        else Hup[i][i-1]=-t;
        if(i-size<0)
             Hup[i][i-size+N]=-t;
            else Hup[i][i-size]=-t ;
}
            /*off diagonal elements*/
for (i=0;i<N-1;i++){
        for(j=i+1;j<N;j++){
            temp=0;
            temp1=0;
            if(V≠0){
            for(k=-4;k≤4;k++){
                for(kk=-4;kk≤4;kk++){
                    row=j/size-i/size+k*size;
                    col=j%size-i%size+kk*size;
                    r=sqrt((double)row*row+col*col);
                    temp+=exp(-r/kappa)/r;
                }
            }
            for(k=0;k<N;k++){
                if((wup[k]-wup[(N-nofh)/2-1])<-1.0e-5)
                temp1+=psiup[k][i]*psiup[k][j];
```

```
                if(fabs(wup[k]-wup[(N-nofh)/2-1])<1.0e-5)
                temp1+=((N-nofh)/2-nofs)/nofd*psiup[k][i]*psiup[k][j];
                }
            }
            Hup[i][j]-=V*temp*temp1;
            Hup[j][i]=Hup[i][j];
        }
}
            for(i=0;i<N;i++){
        for(j=0;j<N;j++){
             Hup[i][j]=(Hup[i][j]
             //+Hup[(i%size)*size+i/size][(j%size)*size+j/size]
             //+Hup[N-1-(i%size)*size-i/size][N-1-(j%size)-j/size]
             +Hup[N-1-i][N-1-j])/2;
        }
}

/*calculate eigenvalues and eigenvectors using LAPACk*/
dsyev_(&jobz,&uplo,&N,Hup,&lda,wup,work,&lwork,&info);
if(info≠0){printf("error");exit(1);}
if(fabs(wup[(N-nofh)/2-1]-wup[N/2-1])<1.0e-5){
                    printf("symmetry broken");
        exit;
}
for(k=0;k<N;k++){
        for(j=0;j<N;j++){
```

```
            psiup[k][j]=Hup[k][j];
        }
    }

    nofd=0; nofs=0;
    for (k=0;k<N;k++){
        if((wup[k]-wup[(N-nofh)/2-1])<-1.0e-5)
            nofs+=1.0;
        if(fabs(wup[k]-wup[(N-nofh)/2-1])<1.0e-5)
            nofd+=1.0;
    }

    for(i=0;i<N;i++)niup[i]=0;
    for(j=0;j<N;j++){
            for(k=0;k<N;k++){
                if((wup[k]-wup[(N-nofh)/2-1])<-1.0e-5)
                niup[j]+=psiup[k][j]*psiup[k][j];
                if(fabs(wup[k]-wup[(N-nofh)/2-1])<1.0e-5)
                niup[j]+=psiup[k][j]*psiup[k][j]
                  *((N-nofh)/2-nofs)/nofd;
        }
    }
    for(i=0;i<N;i++)
        nidown[i+size-1-i%size-i%size]=(niup[i]+niup[N-i-1])/2;
    for(i=0;i<N;i++)
        niup[i]=nidown[i+size-1-i%size-i%size];
```

```
        //for(i=0;i<N;i++)
        // nidown[i]=niup[i+size-1-i%size-i%size];
    }
/*print charge density and spin density*/
    for(i=0;i<N;i++){
        fprintf(spin,"%1.10f",niup[i]-nidown[i]);
        fprintf(density,"%1.10f",1-niup[i]-nidown[i]);
        if(fmod(i+1,size)==0) {
            fprintf(spin,"\n");
          fprintf(density,"\n");
          }
        else {
            fprintf(spin,"\t");
          fprintf(density,"\t");
          }
    }
    temp=0;
    for (i=0;i<N;i++){
        temp+=niup[i]+nidown[i];
        }
/* for (i=0;i<(N)/2;i++){
        printf("%3.16f\n",wup[i]);
        }
*/
    temp1=0;
    for(i=0;i<(N-nofh)/2;i++)temp1+=2*wup[i];
```

```
printf("total energy = %f\n",temp1); //for V≠0
    for(i=0;i<N;i++)temp1-=U*niup[i]*nidown[i];
printf("total charge = %f \n",temp);
printf("total energy = %f\n",temp1); //for V≠0
//printf("%f\t%f\n%d",temp1,temp2,l);
//Coulomb energy
E=temp1;
temp=0;
for(i=0;i<N;i++){
    for(j=i+1;j<N;j++){
        temp1=0;
        for(k=-4;k≤4;k++){
            for(kk=-4;kk≤4;kk++){
                row=j/size+k*size-i/size;
                col=j%size+kk*size-i%size;
                r=sqrt((double)row*row+col*col);
            // printf("%d\t%d\t%f\n",row,col,r);
                temp1+=exp(-r/kappa)/r;
            }
        }
        temp+=V*(niup[i]+nidown[i])
                        *(niup[j]+nidown[j])*temp1;
            }
}
printf("Hartree term=%f\n",temp);
E=E-temp;
```

```
//exchange energy
temp=0;
for(i=0;i<N;i++){
    for(j=0;j<N;j++){
        if(i≠j){
        temp1=0;
        for(k=-4;k≤4;k++){
            for(kk=-4;kk≤4;kk++){
                row=j/size+k∗size-i/size;
                col=j%size+kk∗size-i%size;
                r=sqrt((double)row∗row+col∗col);
                temp1+=exp(-r/kappa)/r;
            }
        }
        temp2=0;
        for(k=0;k<N;k++){
            if((wup[k]-wup[(N-nofh)/2])<-1.0e-5)
            temp2+=psiup[k][i]∗psiup[k][j];
            if(fabs(wup[k]-wup[(N-nofh)/2])<1.0e-5)
            temp2+=psiup[k][i]∗psiup[k][j]
                ∗((N-nofh)/2-nofs)/nofd;
        }
            temp+=V∗temp2∗temp2∗temp1;
        }
        else{
        temp1=0;
```

```
                for(k=-4;k≤4;k++){
                    for(kk=-4;kk≤4;kk++){
                    row=k∗size;
                    col=kk∗size;
                    r=sqrt((double)row∗row+col∗col);
                    temp1=exp(-r/kappa)/r;
                    }
                }
                temp+=V∗niup[i]∗niup[i]∗temp1;
                }
            }
        }
        E=E+temp;
        printf("Exchange term=%f\n",temp);
        printf("total energy=%f\n",E);
}
```

VITA

The author was born in Cangzhou, Hebei, People's Republic of China on February 1, 1971. In September, 1989, he entered Peking University in Beijing, People's Republic of China and received his Bachelor of Science in Physics in July, 1994. In September, 1994, he entered Peking University and received his Master of Science degree in Physics in July, 1997. In August, 1997, he entered Texas A&M University and received his Master of Science degree in Physics in May, 2000. In June, 2000, he entered Texas A&M University and completed the requirements for the Doctor of Philosophy degree in Physics in Dec, 2003.

This document was typeset in LaTeX by the author.